Materials Science & Engineering A 857 (2022) 144091

Contents lists available at ScienceDirect

Materials Science & Engineering A

journal homepage: www.elsevier.com/locate/msea

Effect of heat treatments on the mechanical and microstructural behavior of a hypoeutectic Al alloy obtained by laser powder bed fusion

Jairo Alberto Muñoz [a,b,c,*], Sergio Elizalde [a], Alexander Komissarov [c], José María Cabrera [a,d]

[a] Department of Materials Science and Engineering EEBE, Universidad Politécnica de Catalunya, c/Eduard Maristany 10-14, 08019, Barcelona, Spain
[b] Instituto de Física Rosario, Consejo Nacional de Investigaciones Científicas y Técnicas-CONICET, Universidad Nacional de Rosario, Ocampo y Esmeralda, 2000, Rosario, Argentina
[c] National University of Science and Technology "MISIS", Moscow, 119049, Russia
[d] Fundació CIM-UPC, c/Llorens i Artigas 12, 08028, Barcelona, Spain

ARTICLE INFO

Keywords:
Heat treatment
Al alloy
Laser powder bed fusion
Microstructure
Texture
Plasticity

ABSTRACT

Large gains in strength and ductility are of little significance if the material's anisotropy is high. Therefore, improving the mechanical properties and reducing the anisotropy of Al alloys obtained by additive manufacturing is a topic of growing interest. This manuscript examines the effect of distinct heat treatments on the mechanical, anisotropic, and microstructural behavior of a hypoeutectic, almost eutectic, AlSi11Cu alloy obtained by laser powder bed fusion (L-PBF). The microstructural characterization revealed an Al matrix surrounded by a Si-rich network, forming a coral-like pattern with a heterogeneous combination of columnar and equiaxed grains. The texture indicated that the columnar grains were preferentially oriented towards the building direction with strong Cube and Goss components. Different strength-ductility ratios were obtained following the annealing and solution heat treatments at different temperatures (200 °C–550 °C) with a holding time of 1 h. In terms of grain size and dislocation density, no significant changes were found in the microstructure, suggesting that grain size and dislocation strengthening mechanisms are not highly affected by the heat treatments. In addition, the Si-enriched network remained interconnected until 300 °C. At higher temperatures, this interconnection was lost, giving rise to large Si particles depleting the Si content in solid solution in the Al matrix. Digital image correlation maps revealed that deformation fields were more homogeneous when the cellular structure disappeared. The visco-plastic self-consistent model showed that when applying the load at 30° in the building direction (BD), the largest tensile strength was generated, whereas the lowest strength was obtained when the load was parallel to the BD. Heat treatments for 1 h holding time were found to be efficient in reducing the Lankford coefficients dispersion, suggesting improvements in formability and reducing the alloy's planar anisotropy. These results revealed that annealing up to 400 °C or higher temperatures followed by water quenching leads to good strength and ductility ratios while reducing anisotropy.

1. Introduction

Today, additive manufacturing (AM) technologies have revolutionized new material processing for structural applications [1–3]. This is due to their greater flexibility and reasonable production ratios, reduced amount of wasted material, and low number of manufacturing steps to deliver a nearly finished product after printing [4–6]. The laser powder bed fusion (L-PBF) process stands out from the distinct AM processes. It is one of the most often studied and frequently used in industrial and research centers due to its versatility and speed of adaptation to produce different geometries [7,8]. In this process, pieces are obtained by melting and re-melting consecutive layers of metallic material supplied in powders until the piece is finally shaped with no need for a mold [9,10]. Therefore, this process requires local high temperatures to melt the solid material and join it to the previously applied layers. It has been shown that thermal gradients are generated which influence and determine the material's properties [11]. Some of the consequences of thermal gradients include the formation of high residual stresses and microstructures with large columnar grains with a strong texture and anisotropy [12,13]. The preferential growth direction of columnar

* Corresponding author. Department of Materials Science and Engineering EEBE, Universidad Politécnica de Catalunya, c/Eduard Maristany 10-14, 08019, Barcelona, Spain.
E-mail address: jairo.alberto.munoz@upc.edu (J.A. Muñoz).

https://doi.org/10.1016/j.msea.2022.144091
Received 20 May 2022; Received in revised form 21 September 2022; Accepted 22 September 2022
Available online 27 September 2022

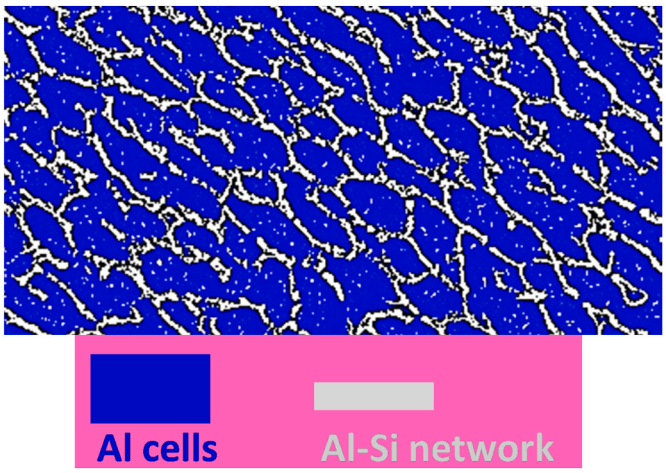

Fig. 1. Cellular structure sketch.

grains during L-PBF of Al alloys is generally parallel to 100 [14].

A wide variety of metallic materials such as titanium alloys, copper alloys, steels, and aluminum alloys have been printed using L-PBF [15–17]. As for aluminum alloys, Al–Si alloys are noteworthy due to their specific strength, corrosion resistance, and weldability, making them ideal for structural applications, especially in the automotive and aerospace industries [18]. Therefore, from an AM point of view, Al–Si eutectic and quasi-eutectic alloys, e.g., Al–12Si, Al–11SiCu, and Al–10Si–Mg, are of interest given their short solidification ranges that reduce the possibility of generating defects such as pores and microcracks and are ideal for counteracting hot cracking [19].

On the other hand, the main drawbacks of Al alloys during AM by L-PBF are their inherent low ductility and anisotropy due to their rigid interconnected structure that is rich in Si and the growth of columnar grains in the building direction, respectively. These phenomena are associated with lower mobility of dislocations and thermal gradients due to the repetitive refusion and fusion of new layers on the already solidified ones [20,21]. In this way, the directional growth of grains, melting pool boundaries (MPB) density, and the obstruction of the dislocation motion generate anisotropy and low ductility in L-PBF materials [22–24]. Xiong et al. [25] found changes in the mechanical properties of an AlSi10Mg alloy depending on the orientation of the melting pools (MPs) related to the load application direction. They concluded that the best strength-ductility combinations were achieved when the load was applied in a direction that is perpendicular to the MPs or BD. Furthermore, Delahaye et al. [24] found that AlSi10Mg alloy fracture occurred in MPBs due to heterogeneity between the heat-affected zone (HAZ) and the interior of the MP. The authors inspected the MPBs in detail, finding that the cellular network was partially broken within the HAZ, permitting easier dislocation slip and plastic strain localization.

In an attempt to solve these issues, some authors have suggested the use of in-situ heat treatments, or heat treatments after the manufacturing process, to improve the performance of materials obtained by AM [26–28]. Heat treatments include annealing to remove residual stresses generated during L-PBF, solution treatment to dissolve precipitates, and aging treatment to harden the alloy through the formation of precipitates and to counteract high cooling rates that promote the formation of high residual stresses. Due to the exceptional L-PBF production conditions, such as the high cooling speeds during solidification, a variety of thermal cycle modifications of traditional heat treatments have been evaluated. For example, Park et al. [29] compared the effect of direct aging and aging after a solution treatment (i.e., T6). It was found that direct aging permitted higher strengths and elongations as compared to the classic T6 hardening treatment. On the other hand, Kempf et al. [30] focused their studies on the effect of post-heat treatments on an AlSi10Mg alloy, taking into account different L-PBF machines. The authors confirmed that the as-built condition determines the final mechanical properties since the same alloy presented different mechanical properties depending on the powder bed fusion devices that were used. Other researchers choose to take advantage of the flexibility of the AM processes to generate in-situ alloys with nanoparticles or other elements during the printing process that allow outstanding mechanical properties to be obtained [31,32]. Another microstructural characteristic responsible for the high strength and low ductility of Al alloys obtained by AM techniques is the formation of an Al cellular structure surrounded by a eutectic Al–Si network (see Fig. 1). In this context, Liu et al. [33] demonstrated that in heat treatment temperatures above 300 °C, fine Si particles precipitate inside the primary Al phase, while at temperatures of the order of 530 °C, larger Si particles appear.

Several studies have been carried out on Al–Si alloys obtained by AM, covering many areas of their behavior. For example, Delahaye et al. [24], examined the influence of Si precipitates on the fracture mechanisms of the material, finding that the HAZ in the MPBs had a lower hardness due to the formation of coarse and non-coherent Si precipitates as failure-initiating areas. Moreover, Pozdnyakov et al. [34] found a thermal expansion coefficient for the AlSi11CuMn alloy manufactured with L-PBF that was similar to the alloy produced from casting in the 20 °C–100 °C temperature range. On the other hand, Nalivaiko et al. [35] studied the synthesis of an AlSi10MgCu alloy by printing single tracks and cubic samples, revealing that low porosity and a uniform microstructure were obtained when using laser powers between 220 and 240 W. As for heat treatments on AlSi10MgCu alloys obtained by AM, Fiocchi et al. [36], in their review work, indicated that the Al–Si alloys obtained by L-PBF experienced a decrease in yield strength with an increase in ductility when applying solution treatments. They also indicated that aging favored strength recovery while maintaining ductility levels similar to those produced by the solution treatment. Regarding anisotropy, a significant problem of Al alloys produced by AM, Rashid et al. [37] reported variations in the properties of an AlSi12 alloy based on energy density and print area. These authors coined the term “energy per layer” (which considers energy density and printing area) as a possible key factor in reducing anisotropy, obtaining fully dense parts.

Although the Al–Si alloys produced by AM have been extensively studied, considerable variation remains with regard to the characterization of their mechanical properties, both in their building state and following heat treatments. In addition, studies on anisotropy have tended to focus on the as-built state, with fewer publications assessing the influence of temperature on texture, plastic behavior, and mechanical properties. Therefore, this study considers printing parameters that have already been shown efficient in producing low porosity in the Al–Si11Cu alloy, focusing on the temperature changes of heat treatments with equal holding time.

Therefore, the study of the microstructural and mechanical characteristics such as texture, strength-ductility ratios, anisotropy, and plastic behavior of AM materials is an active research field. This publication aims to better understand the plastic behavior and anisotropy of the AlSi11Cu alloy through heat treatments at distinct temperatures. To do so, microstructural and mechanical characterization techniques such as optical microscopy (OM), electron back-scattering diffraction (EBSD), and uniaxial tensile tests have been used. Moreover, the visco-plastic self-consistent (VPSC) model was employed to access the material anisotropy in the as-built and heat-treated states.

Table 1
Chemical composition of the studied alloy.

Element	Si	Cu	Mg	Mn	Fe	Ti	Al
Wt.%	9–11	0.8–0.9	0.3–0.5	<0.4	<0.2	<0.2	Bal.

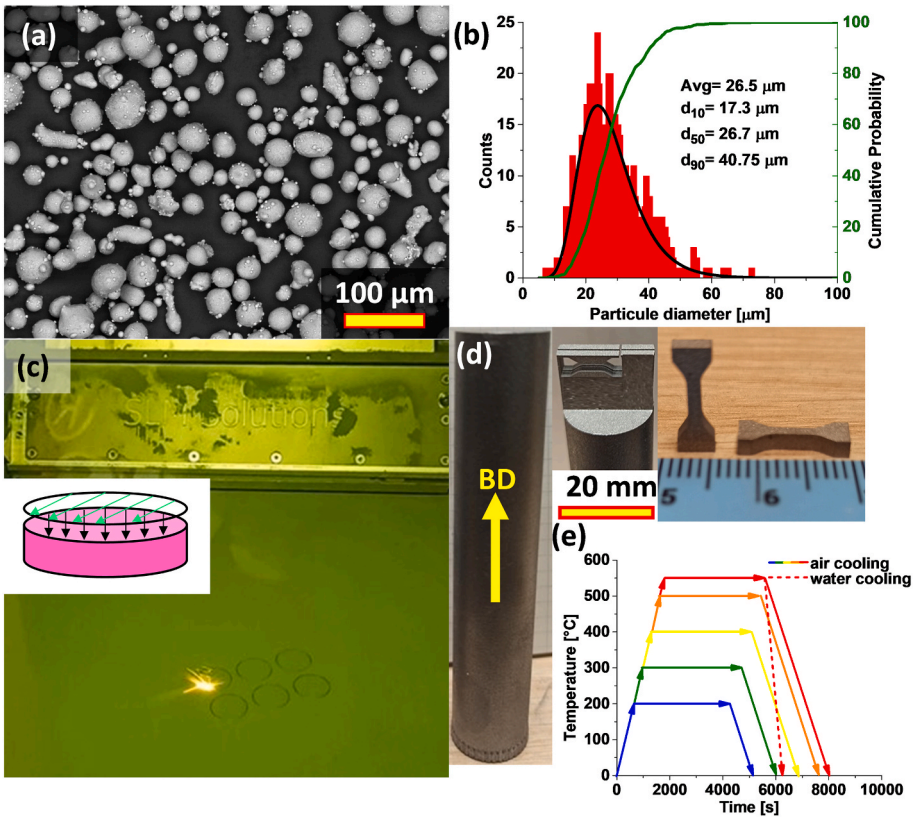

Fig. 2. (a) Powder particles, (b) powder size distribution, (c) L-PBF processing, (d) as-built material and tensile samples orientation, and (e) thermal cycles sketch for the heat treatments.

2. Material and methods

2.1. Initial material and manufacturing methods

Powders with a nominal composition indicated in Table 1 were produced at the Volgograd-Russia Aluminum Plant (UC RUSAL) by the molten metal spraying method.

Fig. 2(a) and Fig. 2(b) display spherical powders with an average size of 26.5 µm following a log-normal distribution (d_{10} = 17.3 µm, d_{50} = 26.7 µm, and d_{90} = 40.75 µm). As illustrated in Fig. 2(c) and (d), cylindrical bars of 20 mm in diameter and 100 mm in length were manufactured by L-PBF in a controlled Argon atmosphere using an SLM280HL printer (SLM Solutions located in Luebeck-Germany). The printing parameters were as follows: scan speed of V = 1650 mm/s, layer thickness H = 50 µm, power of P = 370 W, and hatch spacing of 130 µm, equivalent to a laser energy density (LED) of 1.72 J/mm2 according to the following equation [38]:

$$LED = P/V \times H \quad (1)$$

where P represents laser power, V represents scan speed, and H represents hatch spacing. Printing parameters were selected based on previous studies that show porosities lower than 0.18% [34,39]. The scanning strategy consisted of a 67° rotation after each layer applied (see Fig. 2 (c)).

2.2. Mechanical properties

The material's tensile strength was assessed by uniaxial tests using an Instron universal testing machine at room temperature with a constant strain rate of 1×10^{-3} s^{-1}. Two bone-shaped samples with gauge dimensions of 4 mm × 1.3 mm × 2 mm were cut perpendicularly to the building direction (BD) (see Fig. 2(d)) from the middle length of the rods using electrode discharge machining (EDM). Tensile sample dimensions were scaled from the ASTM D638 standard and cut perpendicular to BD, to avoid MP alignment with the BD. Using digital image correlation (DIC), strain maps and strain profiles were obtained for both the as-built and heat-treated materials. For the DIC analysis, Ncorr software was used, and for the purpose of statistics, a 12-Megapixels digital camera took images every 2 s. Furthermore, Vickers hardness measurements were carried out using a micro-durometer with a square-based pyramidal diamond indenter with face angles of 136°, load of 0.98 N and a dwell time of 10 s.

2.3. Heat treatments

To better understand the thermal stability of the printed alloy, a variety of heat treatments (HTs) were evaluated at different temperatures ranging from 200° to 550 °C, with a holding time of 1 h in an air environment and a constant heating rate of 20 °C/s. Two different cooling media, air and water, were used to evaluate the effect of the cooling rate on the alloy's hardening (see Fig. 2(e)). At this point, the air-cooled annealing treatments were designated based on temperature, for example, 200 °C, 300 °C, 400 °C, 500 °C, and 550 °C. As for cooling in water, the material was designated by the temperature and the cooling medium (i.e., 550 °C water). Subsequently, mechanical behavior and microstructural evolution were examined for each heat treatment. HTs were applied to the printed rods, and then different characterization samples were cut using electrode discharge machining. The samples were immersed in lubricant throughout the cutting process to avoid any rise in temperature.

2.4. Microstructure and texture characterization

Initially, the microstructure of the as-built material was studied by

optical microscopy (OM) using a Zeiss AX10 microscope. The surface of the material was prepared by mechanical grinding followed by electropolishing to eliminate any surface deformation. The electropolishing was performed at 20 kV for 15 s (electrolyte composition: 30% glycerin, 20% HCl, and C_2H_5OH) for subsequent etching using Keller's reagent (2.5% HNO_3, 1% HF, 1.5% HCl, and 95% distilled water). Microstructural characteristics such as the Al cellular structure and Si particle size were analyzed using ImageJ software [40]. For greater detail of the microstructure and composition, a TESCAN VEGA SBH3 scanning electron microscope from Oxford Instruments was used, coupled with an EDS detector (operating conditions, 20 kV and 10 mm working distance). The OM and EBSD samples were extracted from the rod's mid-length in a radial plane containing the BD.

Distinct microstructure characteristics, such as grain size, misorientations, and texture, were quantified by EBSD. The EBSD detector was coupled in an SEM-JEOL JSM-7001F operating at 15 kV, 70° tilt, and with a 15 mm working distance. Samples were prepared as follows: the material's surface was polished using a 2500 sandpaper followed by polishing at 9 μm, 6 μm, 3 μm, and 1 μm diamond suspensions. Then, samples were placed in a vibrating polisher for 2 h using colloidal silica with a particle size of 30 nm. For texture measurements, 900 μm × 900 μm areas were analyzed with a 1 μm step size. The texture was represented as pole figures (PF) and orientation distribution functions (ODF), calculated using the harmonic series expansion method. On the other hand, areas of 400 μm × 400 μm with a step size of 0.5 μm were used to determine different microstructural characteristics. Non-indexed points were corrected using the grain dilation method. Grains with less than two pixels inside were discarded from the statistical analysis. Grain boundaries were divided into low-angle grain boundaries (LAGB) and high-angle grain boundaries (HAGB). Thus, grain boundaries with misorientations between 2° and 15° were considered (LAGB) and those with misorientations greater than 15° were considered HAGB. Data were analyzed using TSL OIM 7.3b and MTEX toolbox software. Image quality (IQ) maps were created to show good contrast between the different types of grain boundaries. These maps describe the quality of a diffraction pattern and they are constructed by mapping the IQ value obtained for each diffraction pattern. Geometrically necessary dislocations (GNDs) were calculated from the 2D-EBSD maps through Nye's tensor using the following equation [41]:

$$\alpha_{ij} = \sum_{n=1}^{N} \rho_{GND}^{n} b_i^n l_j^n \tag{2}$$

where α_{ij} are the Nye's tensor components, b is the Burgers vector, N is the number of types of possible dislocations, and l represents the dislocation line vector. The GND profiles correspond to the point-to-point GND values across a defined line over the GND map.

2.5. Crystal plasticity modeling

The material's plastic behavior was examined using the visco-plastic self-consistent (VPSC) model proposed by Lebensohn et al. [42]. This model considers that each grain deforms differently, analyzing the grain's heterogeneity and anisotropy. The material is represented as a group of grains (grains are treated as ellipsoidal inclusions) with orientations and volume fractions that reproduce the initial crystallographic texture. This model can be applied to aggregates subject to external stresses and strains, especially materials exhibiting anisotropy. This model is described by a nonlinear rate-sensitive equation related to strain rate, D, and stress, S:

$$\dot{\gamma}^s = \dot{\gamma}_0^S \left| \frac{m^s : S}{\tau_c^s} \right|^{\frac{1}{m}} sign(m^s : S)$$

$$D = \sum_s m^s \dot{\gamma}^s \tag{3}$$

Table 2
Voce law hardening values (MPa).

τ^s	τ_0^s	θ_0^s	θ_1^s
55	57	550	0.2

where $m^s = \frac{1}{2}(n^s \otimes b^s + b^s \otimes n^s)$ is the Schmid factor tensor that describes the geometry of each slip system in a crystal, n^s is the normal to the slip plane, b^s is the slip direction, τ_c^s is the critical resolved shear stress (CRSS), $\dot{\gamma}_0^S$ is the reference strain rate, and m is the rate-sensitivity parameter.

Discrete experimental data with up to 5000 orientations were generated from the texture measured by EBSD. For slip dislocations, the 12{111}110 slip systems were considered. For the visco-plastic model, a strain rate sensitivity value of $m = 0.05$ was used. The hardening is described by an extended Voce law as indicated in the following equation [43]:

$$\tau^s = \tau_0^s + \left(\tau_1^s + \theta_1^s \Gamma\right)\left(1 - exp\left(-\Gamma \left|\frac{\theta_0^s}{\tau_1^s}\right|\right)\right) \tag{4}$$

where $\Gamma = \sum_s \Delta\gamma^s$ is defined as the accumulated shear in the grain, whileτ, $\tau_0, \theta_0, \theta_1, (\tau \| 0 + \tau_1)$ represent the resolved shear stress threshold, initial critical resolved shear stress (CRSS), initial hardening rate, asymptotic hardening rate or slope of the plastic region, and the back-extrapolated CRSS represented by the intersection of the slope in the plastic zone with the ordinate, respectively. These values are estimated from a stress-strain plot (for a clearer illustration, see Fig. 1 of [44]). The affine linearization was used for the calculations. The model's fit was carried out through the experimental uniaxial tensile curves for the as-built state. Besides, the simulations were validated by comparing the experimental and simulated pole figures after tensile tests. Table 2 shows the Voce law hardening values used for the material with the greatest homogeneous deformation.

3. Results and discussion

3.1. As-built material

Fig. 3 indicates the Scanning Electron Microscopy (SEM) image and the Energy-Dispersive X-ray Spectroscopy (EDS) of the as-received material in powder form. The composition spectra corroborate a hypoeutectic aluminum-silicon-copper (AlSi11Cu) alloy with other elements such as magnesium, manganese, iron, and titanium.

Fig. 4(a) shows the optical microstructure of the as-built alloy with the BD running parallel to the bars' longitudinal direction. This figure indicates the formation of stacked melting pools (MP). Taking a detailed look at the MP, Fig. 4(b) highlights one melting pool boundary (MPB) in which two zones can be differentiated between the MPB and the interior of the MP. Fig. 4(c) reveals two microstructure characteristics: an interconnected dark network and a light-colored cellular matrix. And within the MPB (red dashed line), there is a more significant expansion of the interconnected network as demonstrated by the SEM image in the yellow box (Fig. 4(d)). In contrast, within the MP (i.e., the yellow box labeled with the letter e), the cellular structure and the interconnected network form a more equiaxed pattern, Fig. 4(e). This behavior may be attributed to the fusion and re-fusion between layers, giving rise to areas in which temperatures reach higher values during the manufacturing process, mainly affecting the MPBs [45]. Thus, the surface of the first solidified MP becomes the area where the new MP will fuse, forming MPBs on which heat is transferred, defining the HAZ.

It can be seen that the light and dark areas illustrated by SEM correspond to Si-enriched and Al cell areas, according to the EDS spectrums in Fig. 4(f) and the study by Rosenthal et al. [46]. Thus, using color threshold separation with ImageJ software, Fig. 4(g) reveals that

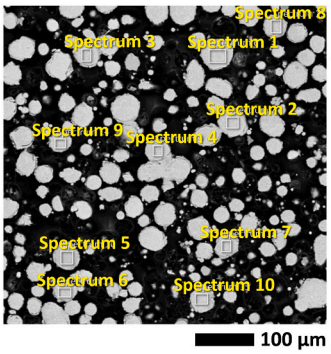

Spectrum Label	Mg	Al	Si	Ti	Mn	Fe	Cu
Spectrum 1	0.55	86.27	11.32	0.27	0.42	0.32	0.85
Spectrum 2	0.51	86.54	11.22	0.21	0.52	0.2	0.8
Spectrum 3	0.51	86.9	10.77	0.17	0.51	0.32	0.82
Spectrum 4	0.59	87.15	10.29	0.35	0.6	0.21	0.81
Spectrum 5	0.59	89.39	9.75	0.04	0	0.13	0.1
Spectrum 6	0.49	87	10.78	0.15	0.65	0.21	0.72
Spectrum 7	0.56	87.5	10.02	0.2	0.53	0.34	0.85
Spectrum 8	0.55	86.39	11.15	0.29	0.54	0.29	0.78
Spectrum 9	0.44	86.98	11.06	0.36	0.42	0.24	0.49
Spectrum 10	0.63	86.35	10.9	0.2	0.67	0.28	0.98
Average	**0.54**	**87.05**	**10.73**	**0.22**	**0.49**	**0.25**	**0.72**

Fig. 3. Chemical composition of the initial powders (all of the values in Wt.%).

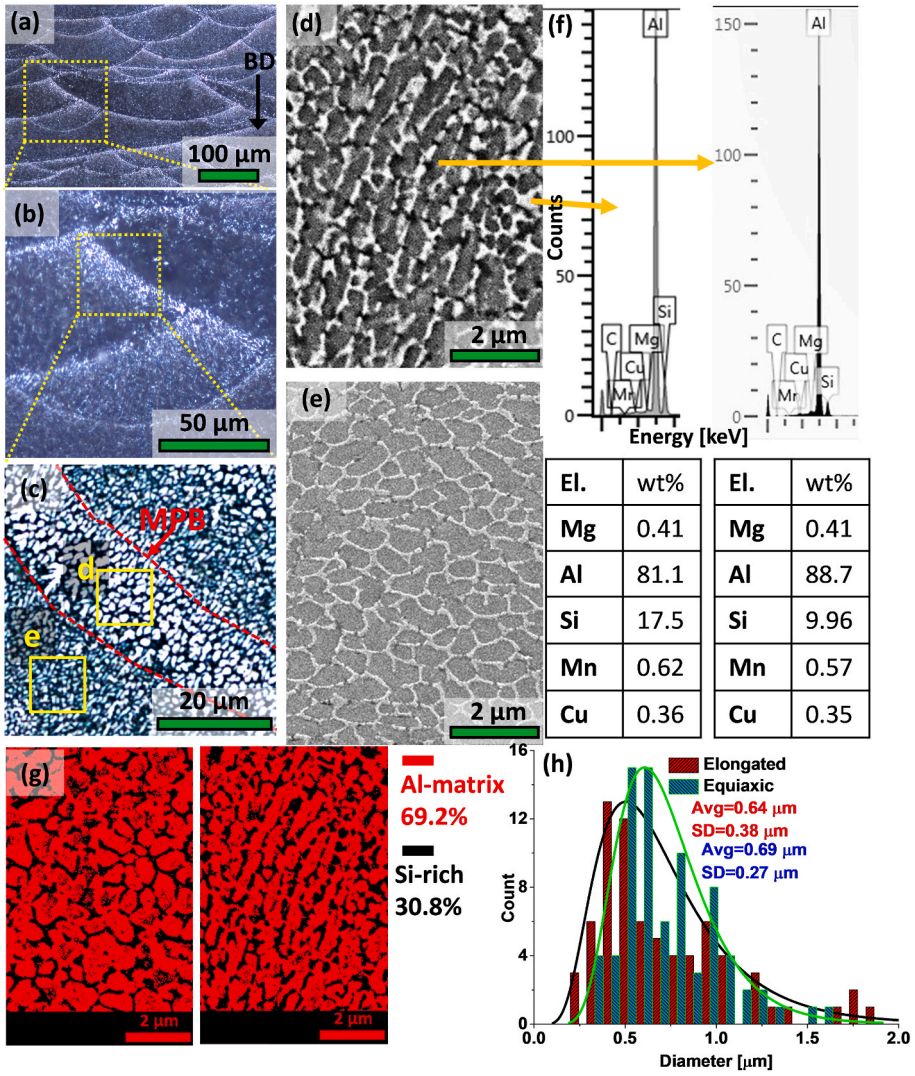

Fig. 4. (a) as-built material optical micrographic, (b) microstructure close to the MPB (c) cellular structure, (d) cellular structure inside the MPB, (e) cellular structure inside the MP, (f) EDS spectra of the interconnected network and cellular structure, (g) Al-matrix and Si-rich area quantification, and (h) cellular structure distributions of the elongated and equiaxed regions.

the area fraction of the Si-rich phase is approximately 30.8%, with the remaining 69.2% corresponding to the primary aluminum matrix. Furthermore, Fig. 4(h) indicates the size distributions corresponding to the equiaxed and elongated cellular structures described in Fig. 4(g). The distributions follow a log-normal function, suggesting that the equiaxed network has a larger average size than the elongated network with values of 0.69 µm and 0.64 µm, respectively.

Therefore, it is clear that the printed alloy consists of an Al matrix and an Si-enriched network. In addition, it is also seen that the MPBs are regions where there is considerable distortion of the Si-rich network due to the more significant thermal gradients occurring in these areas. This behavior suggests the presence of microstructural gradients between the

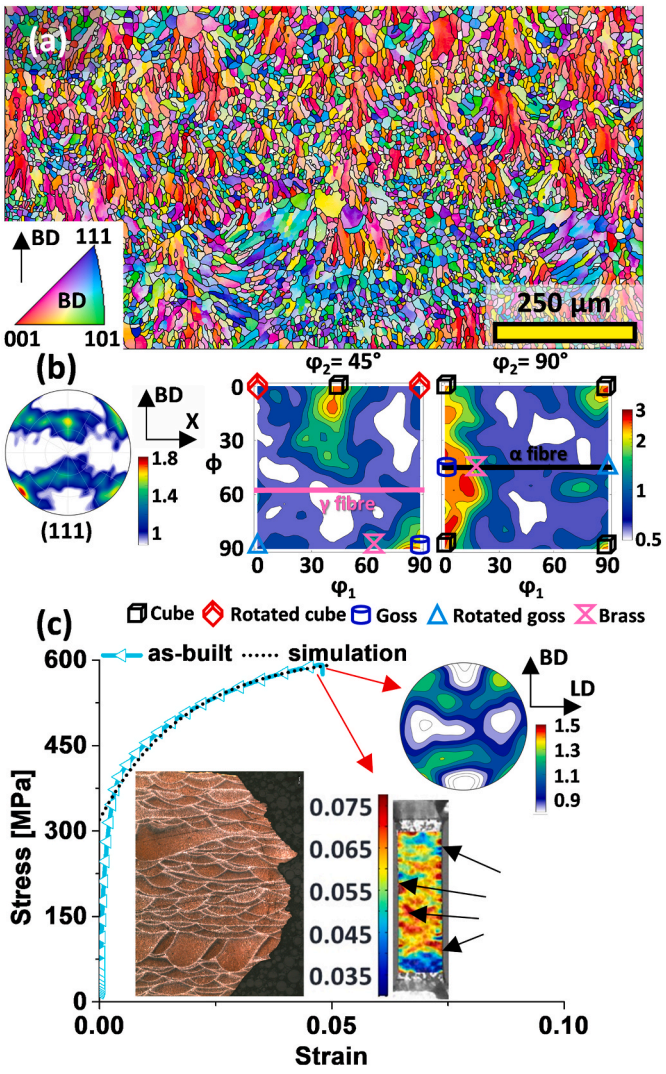

Fig. 5. As-built material properties. (a) IPF colored map, (b) material texture, and (c) tensile curve together with the simulated curve and texture (black arrows indicate multiple strain concentrations).

MPB and the MP interior.

Continuing with the microstructural characterization of the as-built alloy, Fig. 5 indicates the microstructure, texture, and tensile behavior. The inverse pole figure (IPF) map parallel to the BD in Fig. 5 (a) indicates the clear orientation of many crystals in the 001direction. This figure shows a well-defined morphology of columnar grains in the MPs dominated by the previously described texture. According to the PF and ODF sections indicated in Fig. 5(b), this texture can be explained in terms of the development of texture components such as Cube and Goss, which are related to the recrystallization phenomenon [47,48]. For example, Bacroix et al. [49] found that cube-oriented grains were associated with lower dislocation density. In turn, this softening phenomenon can be attributed to the high and heterogeneous temperatures inside the MPs generated during the repetitive solidification processes of new layers, leading to the material's recrystallization, forming a feather-like pattern within each MP. This softening, due to a strong texture component, can be manifested through the anisotropy generated by the numerous elongated grains oriented in the same direction. And, because these grains are the largest, this suggests that the BD orientation is the weakest. These observations permit the visualization of additive manufacturing processes, such as L-PBF, as they induce a heterogeneous microstructure in the material. This behavior is in accordance with the findings of Wu et al. [50], who noted a high fraction of columnar grains after manufacturing an Al alloy. Therefore, it can be established that this behavior corresponds well with material recrystallization, producing elongated grains oriented in the thermal gradient direction [51,52].

As for the tensile behavior of the as-built alloy (i.e., before any heat treatment), Fig. 5(c) reveals an aluminum alloy with a yield strength of 393 ± 9 MPa, a maximum strength of 565 ± 7 MPa, and elongation of 5 ± 1.2 %. These characteristics demonstrate an aluminum alloy with higher mechanical strength than a hypoeutectic Al alloy (Al–7wt%Si) produced by conventional thermo-mechanical methods, such as casting with yield strength values below 100 MPa [53] or even by grain refining through severe plastic deformation (~200 MPa yield strength) [54].

On the other hand, the low ductility of the as-built material is associated with different parameters such as high residual stresses, pores, and cracks generated during the printing process due to high thermal gradients, powder material trapping and pronounced cooling speeds [55,56]. This behavior is manifested by the formation of multiple strain concentration sites where the material can fail. It should also be noted that, although the as-built alloy's ductility is low, the tension loads applied perpendicularly to the BD through the simulated PF reveal the formation of texture changes, with the appearance of components in the load direction (LD). This suggests the microstructure's susceptibility to deformation and possible breakage of the impression texture and grain morphology at higher deformations.

3.2. Texture and microstructure after heat treatments

Fig. 6 permits the visualization of the effect of heat treatments on the as-built alloy's microstructure and texture using EBSD maps and ODF sections for each heat treatment. At first glance, in the IPF maps, it stands out that with the increase in temperature, the strong orientation of the printed grains in the direction 001 ∥ *BD* decreases (see Fig. 6(a) through Fig. 6(f)). Hence, for the temperature range of 200–400 °C, the ODFs in Fig. 6(a)–6(c) indicate a reduction in texture intensity with respect to the as-built material, although the texture of these materials is still dominated by the presence of texture components such as Cube and especially Goss.

At higher temperatures, that is, 500 °C and 550 °C, Fig. 6(d) and (e) indicate an increased intensity of the Goss component, with the Cube component remaining the same as at lower temperatures. With the change in cooling mode, Fig. 6(f) indicates that the Cube and Goss components lose intensity while the Rotated Cube component gains intensity. Thus, it may be observed that after heat treatments, the initial heterogeneous microstructure does not register significant changes in terms of grain growth. There are, however, certain variations in terms of preferential orientation.

Texture, analyzed through EBSD maps, suggests that the microstructural thermal stability of the alloy does not undergo abrupt changes in grain growth. This is related to manufacturing processes that involve temperatures above 550 °C [57], such as L-PBF. Thus, in L-PBF, it is suggested that $T_{manufacturing} > T_{recrystallization-Al}$, giving rise to grains that are not greatly affected by heat treatments, at temperatures reaching 550 °C for 1 h. On the other hand, the maintenance of texture components such as Goss and Cube after heat treatments corroborates the dominance and presence of recrystallized columnar grains, which could change with a different temperature stimulus, such as deformation. This is valid since the ODF weighs the texture component's intensity, considering the number of grains oriented in a specific direction and their area fraction. Therefore, it may be believed that the nucleation of new grains did not occur, and the studied heat treatments affect mainly the Al cellular structure.

Fig. 7(a) to Fig. 7(f) present image quality (IQ) maps following different heat treatments. In these maps, subgrains may be observed in all of the microstructures, especially inside the columnar grains. Once again, this highlights the exceptional thermal stability of the materials processed by L-PBF, suggesting that subgrains are preserved at temperatures above the Al recrystallization temperature. The presence of

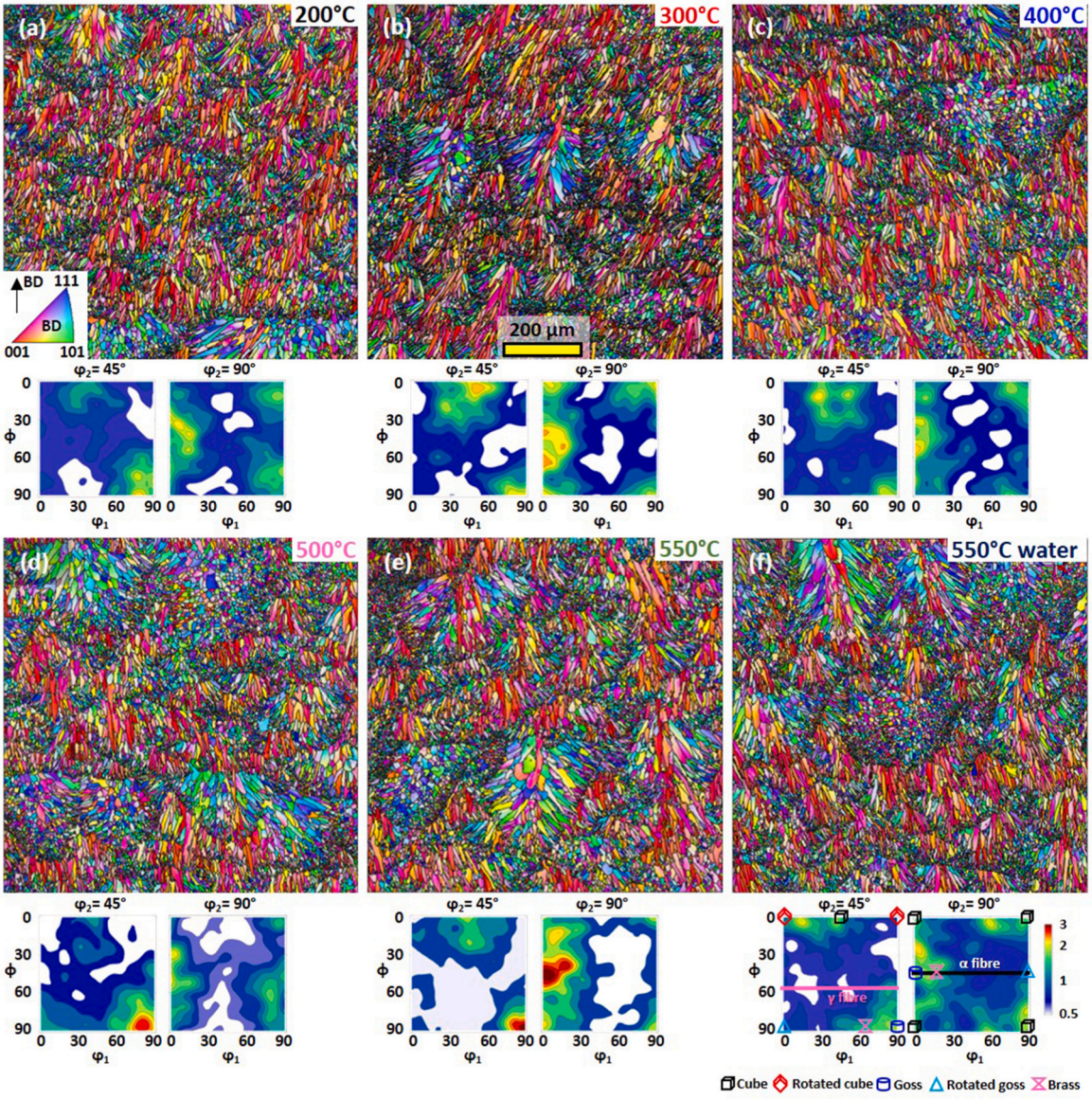

Fig. 6. IPF colored map and texture for the materials following heat treatments. (a) annealed at 200 °C, (b) annealed at 300 °C, (c) annealed at 400 °C, (d) annealed at 500 °C, (e) annealed at 550 °C, and (f) quenched to 550 °C.

low-angle grain boundaries (LAGB) within the columnar grains suggests heterogeneity in misorientation, generating a larger grain curve, that is, a high density of geometrically necessary dislocations (GND) [41,58].

On the other hand, Fig. 7(g) compares the grain size and the aspect ratio of the grains for all of the materials. Here, two elements should be highlighted: 1) grain sizes for the as-built material and the different heat treatments have values of the same magnitude; 2) for grain sizes that are smaller than 10 µm, the as-built material has higher aspect ratio values, and the heat-treated materials indicate higher aspect ratios for grain sizes over 10 µm. Thus, it can be inferred that although heat treatments do not significantly change the average grain size (see Table 3), they do change their shape, especially the larger ones (see Fig. 7(g)). Furthermore, the minor grain growth observed even after 500 °C suggests that the grain boundary strengthening mechanism may have less influence on the resulting material strength in both as-built and heat-treated conditions, as discussed in greater detail in the section on hardening mechanisms.

Cellular structure is another microstructural characteristic influencing the properties of Al alloys manufactured by L-PBF. It can change through heat treatments. Fig. 8 presents the SEM images along with the EDS maps highlighting the main alloying elements for each heat treatment. Initially, SEM images reveal changes in the material's cellular structure. Then, for treatments having temperatures lower than 300 °C, Fig. 8(a) and (b) demonstrate the preservation of the structure with Si being distributed primarily across the interconnected network and Cu following a random distribution. When the temperature rises to 400 °C, Fig. 8(c) indicates that the interconnected network no longer exists, being replaced by multiple, homogeneously distributed particles with high Si content according to the EDS maps. It is worth mentioning that the stability of the interconnected network also depends on the holding time of the heat treatment. For example, Bosio et al. [32] found that cellular structures can break at temperatures lower than 400 °C with times exceeding 5 h during direct aging.

For anneals at 500 °C and 550 °C, Fig. 8(d) and (e) reveal that the Si-rich particles produced by the breakdown of the interconnected network increase in size and become even more Si-enriched. For high-temperature heat treatments and cooling in water, i.e., solubilization heat treatment, Fig. 8(f) indicates that particles have a similar size as in

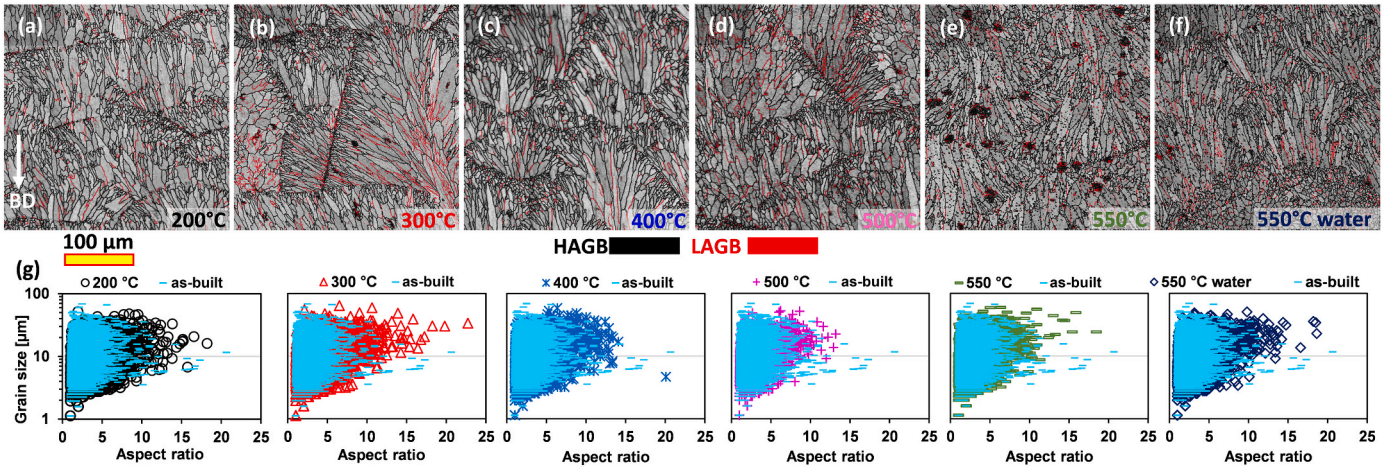

Fig. 7. IQ maps after different heat treatments. (a) 200 °C, (b) 300 °C, (c) 400 °C, (d) 500 °C, (e) 550 °C, (f) 550 °C water, and (g) grain morphology for the different heat treatments.

Table 3
Microstructure properties.

Material	Grain size [µm]	Area % Si-rich phase	Cellular and particle size [µm]	% HAGB	Average misorientation [°]
as-built	5.35 ± 3.2	30.8	0.66 ± 0.38	86	33.6
200 °C	5.87 ± 3.0	24.3	0.62 ± 0.4	85	33.6
300 °C	6.29 ± 3.5	27.4	0.6 ± 0.48	79	30.9
400 °C	5.98 ± 2.8	40	0.21 ± 0.17	82	31.2
500 °C	6.62 ± 2.5	27	0.81 ± 0.61	70	27.8
550 °C	4.98 ± 1.9	15.6	1.06 ± 0.56	84	34.8
550 °C water	5.2 ± 1.3	12.5	0.99 ± 0.7	84	34.2

the air-cooling treatment shown in Fig. 8(d), although with different shapes. Rapid cooling in water produces particles with less circularity and straight edges. According to Kempf et al. [30], cellular network destruction is consistent with temperature increments that cause a reduction in the Si content in solid solution due to its expulsion from the Al matrix. This solute migration confirms the formation of a supersaturated solid solution after manufacturing through the L-PBF process. This is consistent with the Si diffusivity coefficient, which is greater than aluminum's self-diffusion coefficient, meaning that Si diffuses faster than Al in this type of alloy, forming Si-enriched particles [59]. Also, Mg has a higher diffusivity coefficient than Al; however, we do not observe a clear distribution of this element by EDS as in the case of Si due to its lesser quantity and since it may form nanometric precipitates that cannot be observed with SEM. On the other hand, elements such as Fe and Mn have a lower diffusion coefficient than Al.

3.3. Mechanical properties

The result of heat treatments on microstructure and its influence on the alloy's mechanical properties is analyzed with uniaxial tensile tests. Fig. 9 summarizes and compares the mechanical properties in the as-built state and following distinct heat treatments. Fig. 9(a) shows the tensile curves for all materials together with the simulated curves using the VPSC model. With the heat treatments, the alloy indicates a ductility improvement at the cost of its strength. Fig. 9(b) reveals various strength and ductility values that decrease and increase, respectively, with increasing annealing temperature. However, heating the alloy at 550 °C and cooling in water produces intermediate properties between annealing at 300 °C and 400 °C. The reduced elongation following the annealing and quenching at 550 °C can be associated with the embrittlement effect due to the migration of larger solutes (mainly Si atoms) from the Al matrix to the particles, as discussed in the following sections.

The tensile strength evolution is consistent with the material's corresponding microstructure. For heat treatments up to 300 °C in which the cellular network is maintained, only changes in strength occur with ductility that is very similar to that of as-built material. On the contrary, when the cellular network is broken and uniformly distributed particles are formed ($T > 400$ °C), the material undergoes reductions in strength with homogeneous deformations greater than 15%. It should be noted that when the solutionization treatment is applied, better strength-ductility ratios than annealing at 550 °C are obtained (see Fig. 9(b)). This can be attributed to the generation of texture components such as Rotated cube and the formation of non-circular shaped particles with lower Si content due to rapid cooling in water. The lower elongation in the sample annealed at 200 °C as compared to the as-built state may be related to defects such as micropores or scratches from the melting and cutting process, respectively. Kempf et al. found cracks and pores (metallurgical and keyholes) on the fracture area surface of an AlSi10Mg after annealing at 300 °C [30]. According to the hardness values presented in Fig. 9(c), the quenched material attains hardness values that are greater than those of the other tested conditions, even the as-built one. This verifies that rapid cooling does not favor the excessive growth of precipitates and gives less time for the release of Si in solid solution than cooling in air. Furthermore, the fast cooling rate could have a lower impact on the nanoprecipitates than the slow annealing cooling rate.

Fig. 9(d) compares the tensile properties of the as-built alloy with those obtained from casting and a combination of rolling with severe plastic deformation (SPD) processes such as Equal Channel Angular Pressing (ECAP). At first glance, the as-built and heat-treated alloy strength and ductility values are higher than the Al–11Si alloy in the as-cast, cast + rolling, and ECAP + rolling conditions reported by Son et al. [60]. Accordingly, the annealing treatments demonstrate a wide variety of mechanical properties with remarkable strength-ductility combinations over SPD techniques.

Thus, the great potential of additive manufacturing technologies to offer a new generation of materials has been verified. Furthermore, L-PBF permits the creation of heterogeneous and tougher materials having characteristics that are distinct from those obtained with traditional processes.

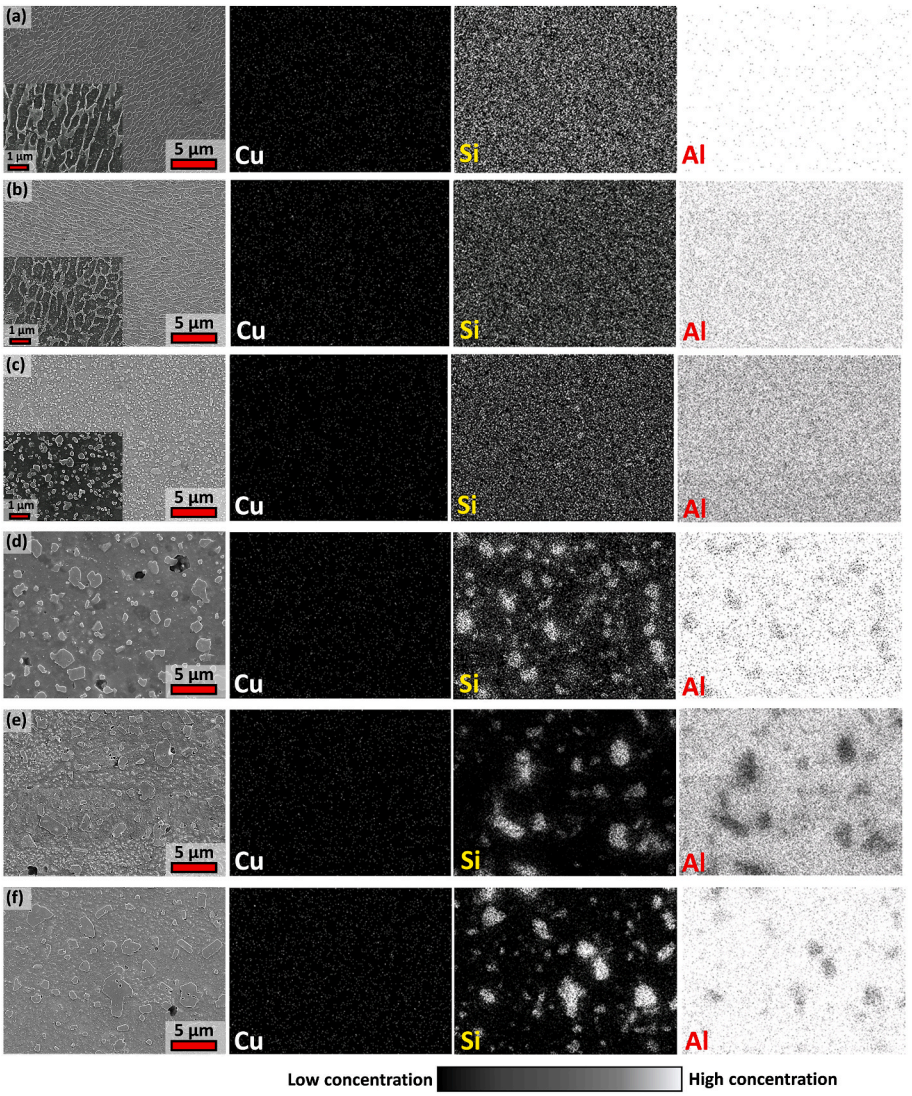

Fig. 8. SEM and EDS maps for the heat-treated materials. (a) 200 °C, (b) 300 °C, (c) 400 °C, (d) 500 °C, (e) 550 °C, and (f) 550 °C water.

3.4. Strain distribution and changes in the cellular network

Fig. 10 presents the strain profiles along with the tensile specimens before fracture. Video 1 summarizes all of the tensile tests indicating the changes in strain distribution and the evolution of the average strain. For the as-built material and with annealing temperatures below 300 °C, the strain profiles and tensile tests reveal a heterogeneous strain concentration. This behavior is associated with the microstructures indicated in Fig. 8, where the interconnected Si network is maintained up to 300 °C. Hence, the heterogeneous distribution of deformations can be associated with the multiple connections of the interconnected network that act as stress concentration points. Thus, the interconnected network walls do not permit significant movement of dislocations since they can reduce dislocation mean free path, causing material hardening through dislocation pile-ups and, simultaneously, multiple stress concentration points during the tensile test. Furthermore, the texture indicated in Fig. 5(b) and Fig. 6 demonstrates that up to the heat treatment of 300 °C, the components are very similar to those of the as-built material. The heterogeneous state of deformation is manifested by high strains concentrated in small areas generating serrated deformation profiles, Fig. 10(a) through Fig. 10(c). Then, the multiple strain concentration points interconnect to form multiple strain bands before fracture as shown in Video 1. Thus, annealing treatments with temperatures below 300 °C do not significantly alter ductility. However, when the heat treatment temperature exceeds 400 °C, and the interconnected cell structure breaks down, the strain profiles and maps before fracture, indicated in Fig. 10(d) and (e), and Video 1, confirm that the strain is concentrated in a specific area at the end of the test. This behavior is represented by a single peak strain profile, allowing more significant elongation before fracture, as indicated in Fig. 9. Thus, the breaking of the Si-enriched network, as indicated in Fig. 8, reduces the material strength while simultaneously generating more space for the movement of dislocations, permitting higher fracture strains, according to Fig. 9.

Supplementary video related to this article can be found at https://doi.org/10.1016/j.msea.2022.144091

For heat treatments at a temperature of 550 °C, Fig. 10(f) and (g) indicate plateau-type strain profiles with the strain being distributed more evenly over the entire length of the tensile specimen at the end of the test. Rapid cooling from a temperature of 550 °C results in not only a more homogeneous strain distribution over the entire length tested, but also a good combination of strength and ductility. Although both treatments at 550 °C generate similar deformation profiles, the marked difference in the strength-ductility relationship is associated with the type of cooling, which generates different amounts of Si in solid solution and particles of different sizes, as shown below.

The effect of temperature on the transformations of the Si-rich cell

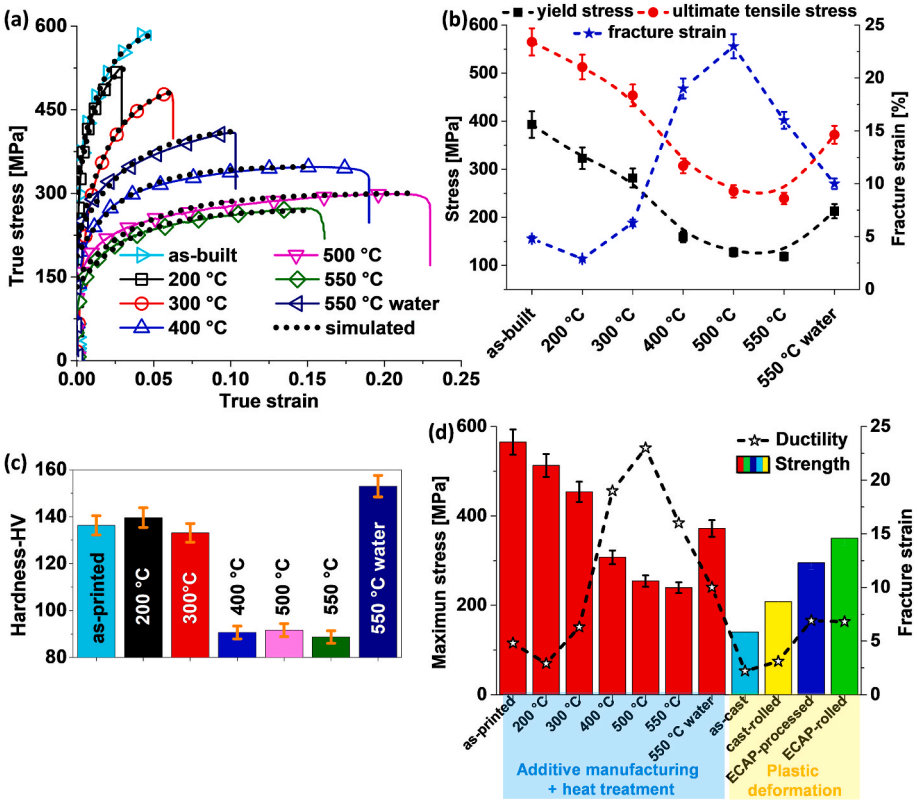

Fig. 9. (a) experimental tensile curves (continuous symbol lines) for the as-built and heat-treated materials together with the simulated curves (dotted lines), (b) strength-ductility evolution, (c) hardness values for all of the tested materials, and (d) mechanical properties comparison with other processing techniques such as equal channel angular pressing (ECAP), rolling, and as-cast [60].

network is shown in Fig. 11. Temperatures lower than 300 °C permit the cell network to be maintained with minor Si content increments, Fig. 11 (a) and (b). On the contrary, the heating of the alloy above 400 °C produces a breakdown of the cellular network that gives rise to a distribution of homogeneous particles that grow in size with increasing temperature (see Fig. 11(c)–11(f)). Furthermore, in Fig. 11(g) it is observed that cellular structure size for annealing treatments at 200 °C and 300 °C does not change abruptly in the as-built material, as indicated in Fig. 4(h). From the breakdown of the cellular structure, that is, annealing heat treatment at 400 °C, the microstructure changes to a homogeneous distribution of Si-rich particles having an average size of 0.21 ± 0.17 μm, reaching sizes greater than 1 ± 0.56 μm above 550 °C. Thus, as the particles grow, their density decreases, increasing the separation between them. This behavior can be better described by the critical radius equation of nucleation (R) [61]:

$$R = \frac{2\gamma\vartheta_{at}}{k_B T ln\left(C/C_{eq}\right)} \tag{5}$$

where γ is the interface energy between the matrix and the precipitates, ϑ_{at} represents the volume of atoms, k_B is the Boltzmann constant, T is the temperature, C is the instantaneous solute concentration, and C_{eq} the balanced concentration of solute in the matrix. When the heat treatment is applied on the alloy, the exsolution of solute atoms from supersaturated solid solution occurs, and the nucleation of precipitates is thereby initiated. Eq. (5) shows an inversely proportional relationship between the critical radius and the temperature; the higher the temperature, the lower the critical radius, indicating the coarsening of precipitated phases. Furthermore, when the nucleation process ends, the particles can grow by absorbing smaller particles in their proximity [26]. Thus, fewer particles with an increased area are generated following an Ostwald ripening mechanism. According to Du et al. [62], the growth of precipitates in Al alloys subjected to annealing can be described by the Lifshitz–Slyozov–Wagner model, according to the following equation:

$$R^3 - R_0^3 = Kt \tag{6}$$

where R and R_0 represent the initial and final size of the precipitated particles, t is the time, and K is the growing coefficient described by the equation below [62]:

$$K = \frac{8\vartheta_{at}^2\gamma C_{eq} D}{9k_B T} \tag{7}$$

where $D = D_0\, exp\left(\frac{-Q}{RT}\right)$ is the solute diffusion coefficient, D_0 is the initial diffusion coefficient, Q the activation energy, Trefers to temperature, and R is a constant (8.31 Jmol K^{-1}).

Given that in this study, all of the treatments used the same holding time, the growth of the particles is more significant when there is more diffusion, which is favored at higher temperatures. Solute migration from the Al matrix towards the particles increasing their weight percentage from 11% Si to 17% after treatment at 550 °C is reflected in the Si content indicated in the SEM images of Fig. 11 and Fig. S1 of the supplementary material. However, rapid cooling media permit particles of a lower Si quantity, producing a quenched material with a greater strength than in air-cooled condition. For this reason, Si-rich particles are larger in air cooling than in water cooling, as illustrated in Fig. 11(g). Therefore, the high strength and low ductility of the as-built material are related to the Si interconnected network that serves as a barrier to the movement of dislocations and the supersaturated Al solid solution. Later, when the cellular network breaks and Si- enriched particles appear, the material strength decreases while the ductility increases due to the additional space for the movement of the dislocations, which increases with the growth of the Si-rich particles. Therefore, the mean free path for the movement of the dislocations increases. Zhang et al. [63] demonstrated that the AlSi3.5Mg2.5 alloy subjected to direct aging

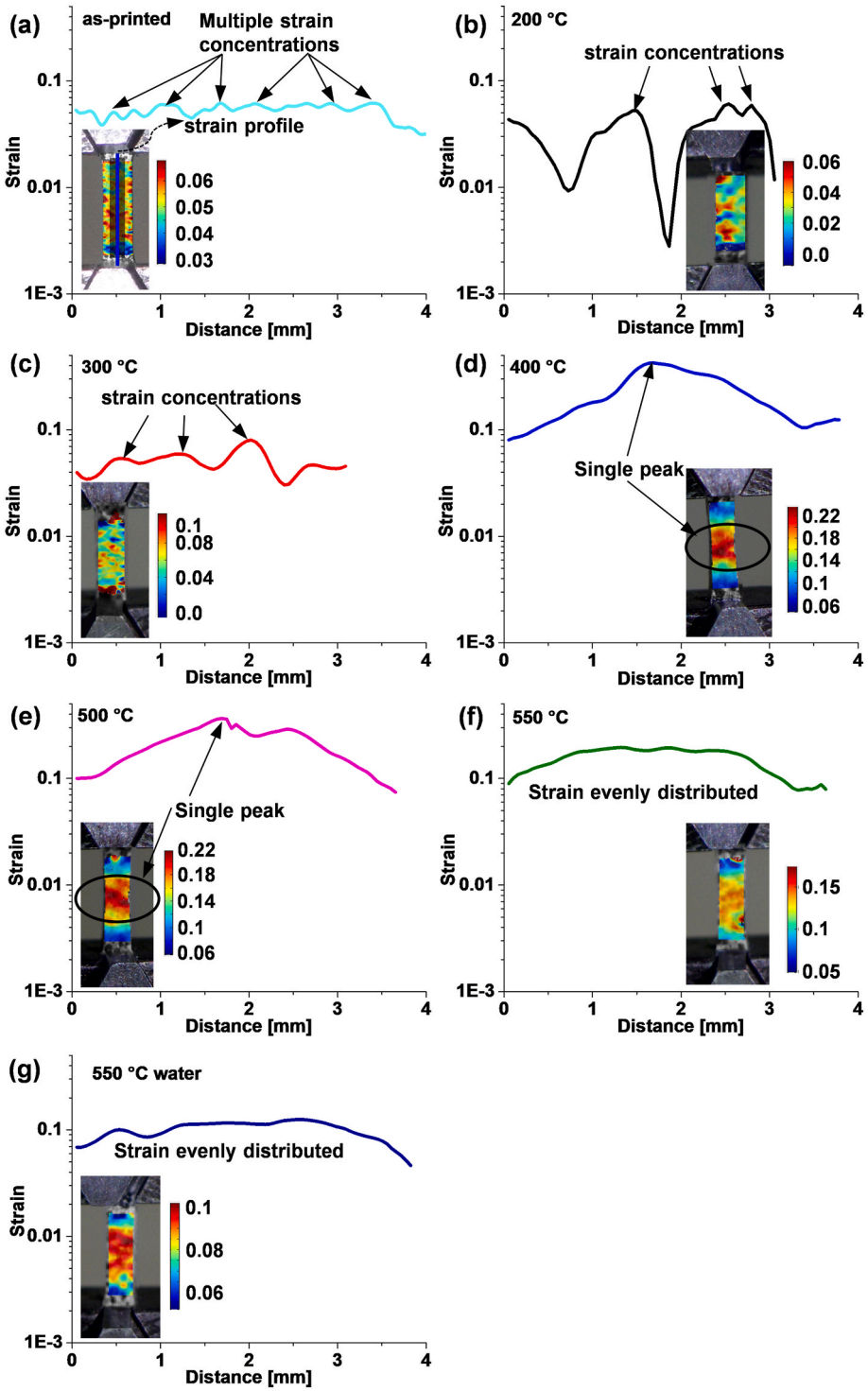

Fig. 10. Strain maps and strain profiles before fracture for all of the materials. (a) as-built, (b) 200 °C, (c) 300 °C, (d) 400 °C, (e) 500 °C, (f) 550 °C, and (g) 550 °C water. (Strain profiles were obtained along the tensile samples' longitudinal direction as indicated by the blue line in Fig. 10a). (For interpretation of the references to color in this figure legend, the reader is referred to the Web version of this article.)

exhibited greater dislocation generation and annihilation rate than in the as-built state. This behavior was attributed to the fact that after direct aging, the isolated precipitates presented weaker constrictions for dislocations than the cell boundary network in the as-built state.

Thus, for the range of temperatures tested and the constant time, there are no significant changes in the grain size (see Table 3), and the mechanical properties of the materials depend greatly on the state of the cellular network and the solute atoms in the Al matrix. However, when the network changes to large particles, the hardening contribution of both precipitates and solid solution elements can be significantly penalized due to the growth of the precipitates and the migration of solid solution elements towards the particles. In this context, Santos Macías et al. [28] demonstrated that using a temperature of 200 °C during the printing of an AlSi10Mg alloy increases the precipitates size as well as some disconnections in the cellular network affecting the alloy strength, unlike that manufactured at room temperature.

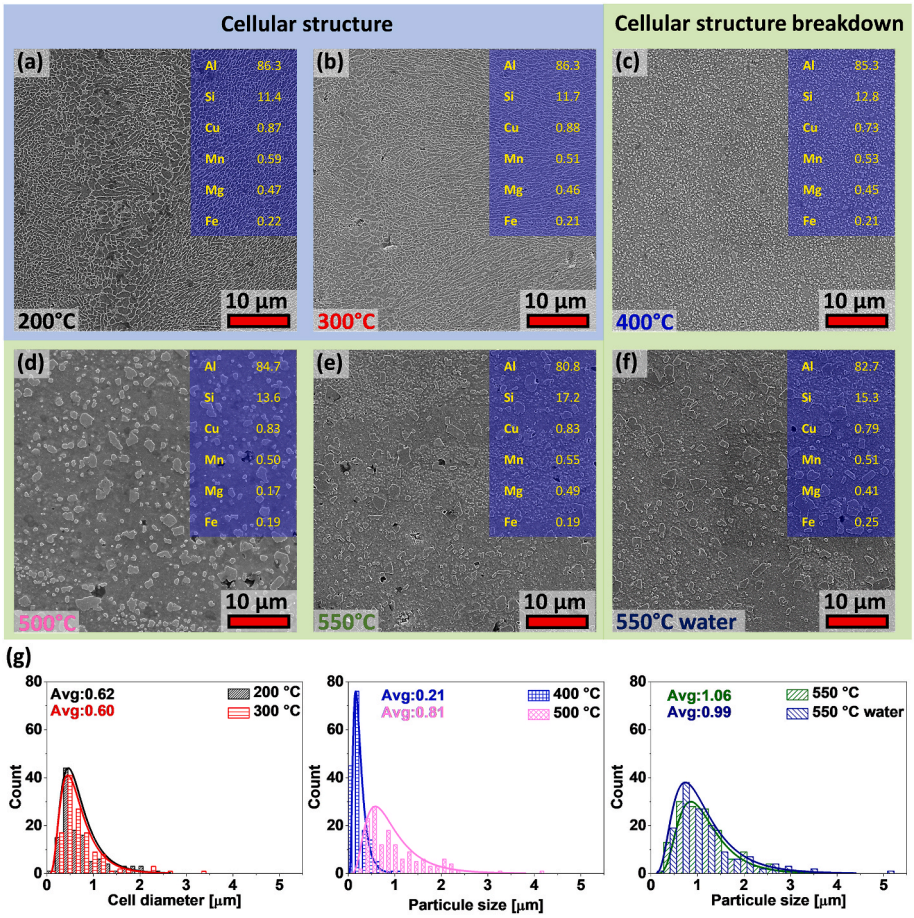

Fig. 11. SEM images and compositions for the heat-treated materials. (a) 200 °C, (b) 300 °C, (c) 400 °C, (d) 500 °C, (e) 550 °C, (f) 550 °C water, and (g) cellular and particle size distributions. (The compositions correspond to the interconnected structure and the particles after the network broke).

To better understand the mechanical properties of the Al alloy in the as-built state and after the different heat treatments, the distinct hardening mechanisms are discussed below.

3.5. Hardening mechanisms

In terms of the strengthening mechanisms, several authors have established that the strength of Al–Si alloys obtained by AM is the sum of the Si- enriched network and the Al cellular structure contributions according to the following equation [28,64]:

$$\sigma_y = f_{cell}\left(\sigma_o + \sigma_{preci} + \sigma_{ss} + \sigma_{disloc} + \sigma_{bound}\right) + f_{net}\sigma_{load} \tag{8}$$

where f_{cell} and f_{net} represent the fractions of the cellular and Si-enriched network, respectively. With f_{cell} and f_{net} satisfying that: $f_{cell} + f_{net} = 1$. On the other hand, the components σ_o, σ_{preci}, σ_{ss}, σ_{disloc}, σ_{bound}, and σ_{load} represent the contributions of the friction stress, precipitates, solid solution, dislocations, Si-network boundaries, and the Si network load capacity, respectively. Each contribution follows the equations below:

$$\sigma_{preci} = \frac{MGb}{l} \tag{9}$$

$$\sigma_{SS} = kC^{2/3} \tag{10}$$

$$\sigma_{disloc} = \alpha MGb\sqrt{\rho} \tag{11}$$

$$\sigma_{bound} = \frac{k_d}{\sqrt{d_{net}}} \tag{12}$$

where M is the Taylor factor, G the shear modulus, b the Burgers vector, l the particle spacing in the slip plane ($l = \frac{d_{preci}}{2}\sqrt{\frac{2\pi}{3f_v}}$), d_{preci} the precipitates diameter, f_v the volume fraction of particles, k a constant for Si, C the concentration of Si in solid solution, α a dislocation hardening constant, ρ the dislocations density ($\rho_{total} = \rho_{GND} + \rho_{Statistically stored}$), and k_d the thickness of the Si-rich network, which can be considered the diameter of the Al cells (d_{net}).

Since the cellular network is maintained to heat treatment of 300 °C, as shown in Fig. 11, it is valid to use Eq. (8) to describe the alloy's yield strength. However, as of 400 °C, when the cellular network breaks and there is a pronounced decrease in strength, the boundaries and the cellular network load tend to be less relevant. Therefore, Eq. (8) can be simplified to the classical equation used to describe the strength of conventionally produced alloys. That is, $\sigma_y = \sigma_o + \sigma_{preci} + \sigma_{ss} + \sigma_{disloc}$.

Although the material is subjected to high temperatures during the manufacturing process, the high density of dislocations in additive manufactured metallic materials has yet to be clearly explained. Some authors have suggested that its origin is independent of the metallic system and depends on the AM process—for example, the thermal inhomogeneity generated during melting gives repetitive stress-compression cycles, which are considered to be the major contribution to high-density dislocations [65].

Regarding dislocations, we have described the hardening contribution of dislocations based on the GND magnitudes calculated by EBSD. These dislocations are part of the overall number of dislocations in the material, and they are related to subgrain development (i.e., misorientation variations) and crystal curvature. Hence, we cannot assess the absolute magnitude of dislocation density, but we can infer the effect of

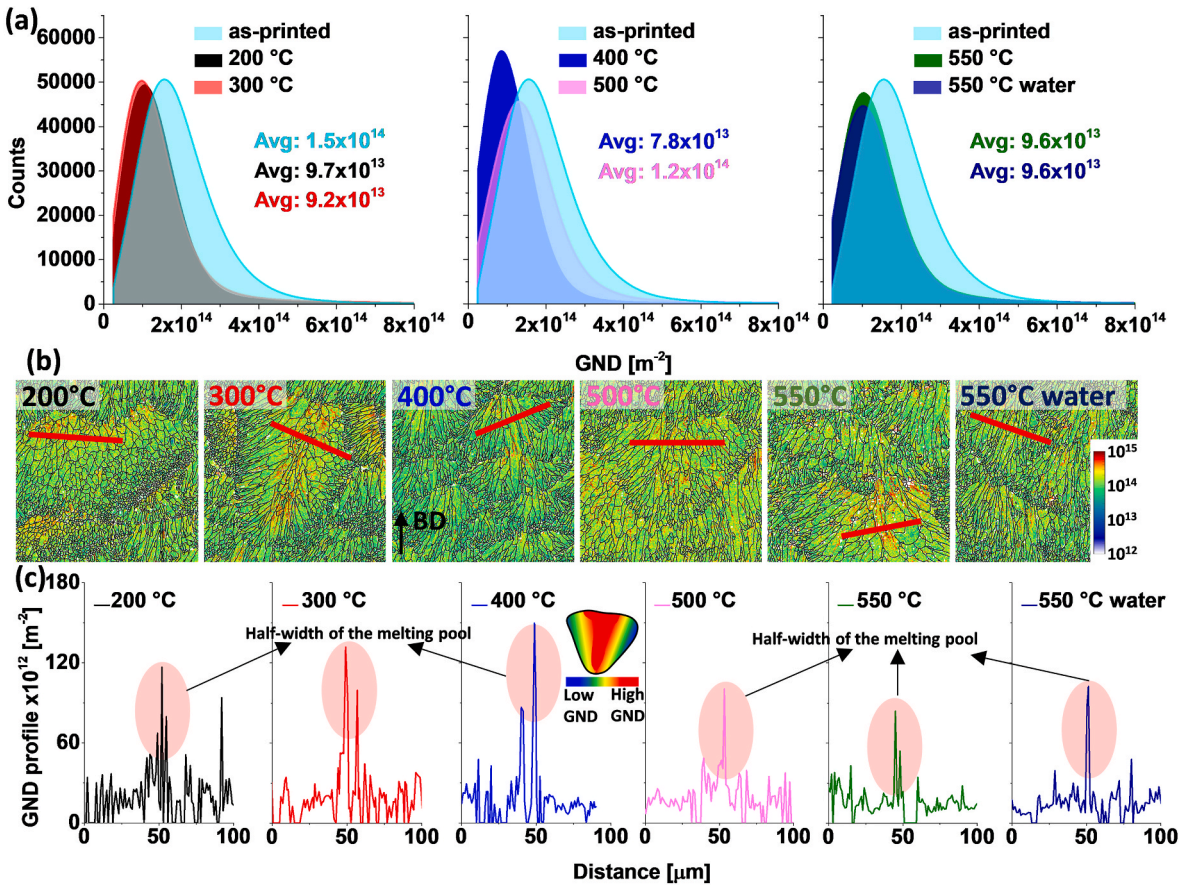

Fig. 12. (a) GND distributions, (b) GND maps, and (c) GND profiles across the melting pool width (red lines in GND maps) and GND sketch indicating the zones with low and high GND densities within the MP. (For interpretation of the references to color in this figure legend, the reader is referred to the Web version of this article.)

heat treatment on the dislocation hardening mechanism. Thus, contrary to the evident recovery, recrystallization, dislocations annihilation, and increased misorientation occurring in Al alloys produced by traditional methods when subjected to high temperatures [47,66]; the alloy produced by L-PBF shows no significant changes in grain size, HAGB fractions, and average misorientation (see Table 3) even after annealing at 550 °C. This behavior reveals that the hardening contribution magnitude from dislocations should not change considerably following the heat treatments, as evidenced in Fig. 12 with the GNDs evolution indicating similar magnitudes. For example, Santos Macías et al. [28] reported no change in the dislocation hardening contribution when they manufactured an AlSi10Mg alloy using two different build platform temperatures. They also found that the dislocations' hardening contribution was the second lowest after the friction stress.

In the present investigation, dislocation strengthening begins to be more representative of the alloy yield stress as the annealing temperature increases. This is because other hardening mechanisms such as the interconnected network, solid solution, and precipitates are less effective, almost negligible when the annealing temperature is high (in this study, temperatures above 300 °C). Moreover, since GNDs quantify the curvature and grouping of dislocations in the LAGBs, their behavior can be an excellent indicator of the alloy's grain size stability. Thus, Fig. 12 (a) indicates a reduction in GND density after heat treatments relative to the as-built material, demonstrating that the alloy does not experience strong recovery or recrystallization after the heat treatments.

Another relevant aspect of GNDs is their distribution within the microstructure, as shown in Fig. 12(b). These maps allow us to appreciate their heterogeneous distribution, with the highest densities occurring within the largest grains. According to Muñoz et al. [14], the anisotropy induced by the L-PBF process generates columnar grains oriented to the BD, with GND densities being dependent on measurement direction. For clarity, Fig. 12(c) plots the GND profiles across the width of the melt pools (red lines in Fig. 12(b)). These profiles confirm that a peak occurs at the half-width of the MP, where more GNDs are piled. Therefore, the higher GND densities are located in the middle zone and they decrease as they approach the MPB, as shown in the sketch in Fig. 12(c). Therefore, there are more significant plastic gradients in the perpendicular direction than parallel to the BD. This behavior reveals the anisotropy of the alloy in correspondence with the columnar grains indicated in Fig. 6.

Other hardening mechanisms such as precipitation and solid solution are also affected by temperature. According to Eq. (9), the precipitate hardening is inversely proportional to the spacing between precipitated particles, which in turn depends directly on the diameter of the precipitates [31]. Therefore, the increase in temperature causes the precipitates to increase in size, making their mean distance larger, as described in the previous section and indicated in Fig. 11. In addition, as shown by the EDS of Fig. 11, with increasing temperature, more significant amounts of Si are observed in the particles, demonstrating the depletion of Si in solid solution, which decreases the contribution from the solid solution according to Eq. (10). On the other hand, rapid cooling from 550 °C is found to produce better strength than air cooling due to the lower Si migration to the particles. Thus, slow cooling leads to more notable deterioration of the hardening mechanisms as compared to water cooling. Therefore, according to several investigations of Al alloys [61,62], it is seen that the growth of Si-enriched particles is a function of the diffusion rate, which increases with temperature (as shown in Eq. (7)) but decreases with faster quenching.

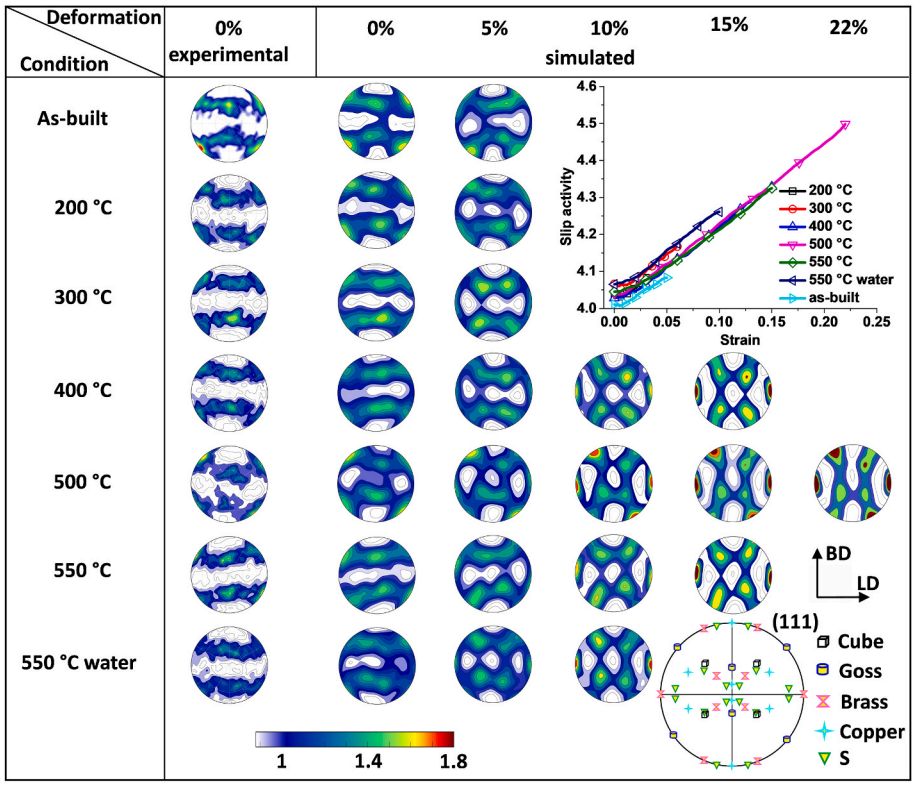

Fig. 13. Texture evolution simulation during the tensile tests for all of the materials with the loading direction (LD) perpendicular to BD.

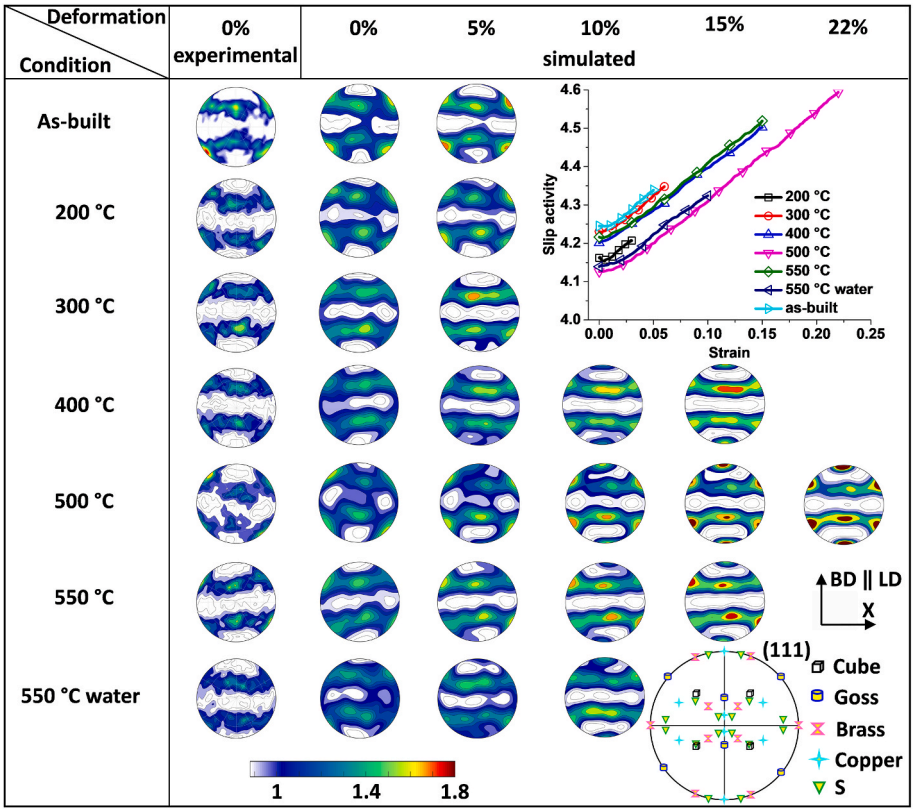

Fig. 14. Texture evolution simulation during the tensile tests for all of the materials with the loading direction (LD) parallel to BD.

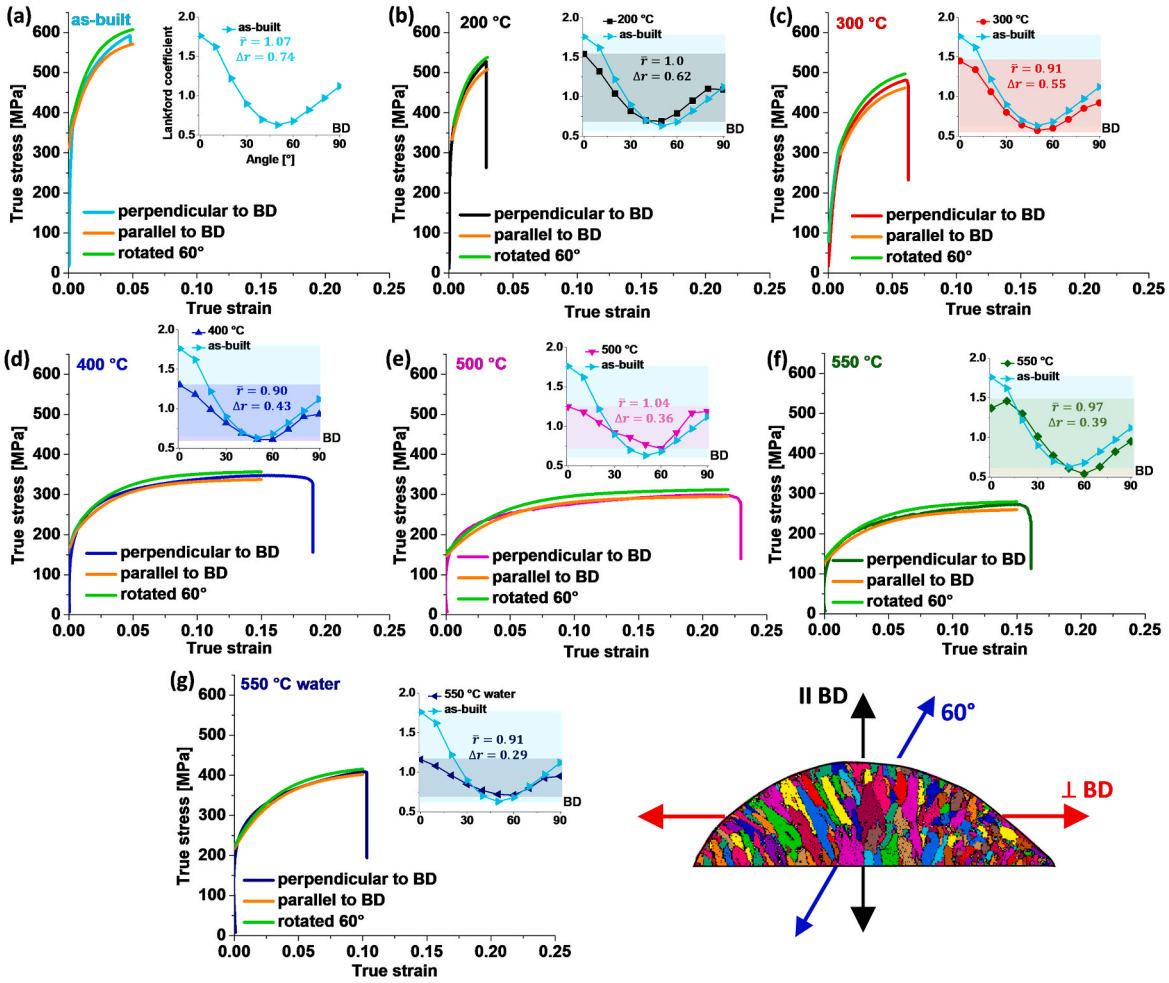

Fig. 15. Predicted tensile curves with different orientations and Lankford coefficient for all of the materials. (a) as-built, (b) 200 °C, (c) 300 °C, (d) 400 °C, (e) 500 °C, (f) 550 °C, and (g) 550 °C water.

3.6. VPSC simulations

The anisotropy study of metallic materials produced by 3D printing is critical for its successful application [67,68]. Simulations using the VPSC model predicted tensile curves at different orientations. Thus, the Lankford coefficients were calculated.

Fig. 13 and Fig. 14 indicate the simulated texture changes at different levels of deformation during the tensile test, considering the applied load that is parallel and perpendicular to the BD, respectively. Thus, the simulated texture evolution for the tensile tests shows a good correlation with the experimental texture measured after the tensile test, as seen in Fig. S2 of the supplementary material.

At first glance, Fig. 13 shows that 5% tensile deformation changes the texture concerning the as-built material when the load direction (LD) is perpendicular to the BD. After the breakdown of the Si-enriched network (i.e., $T > 400$ °C), more significant deformations are reached, leading to substantial changes in alloy texture. Thus, deformations larger than 10% go from an initial texture dominated by the Goss component to a texture in which the Brass and Cube components dominate. For example, the material annealed at 500 °C indicates that the Brass component begins to form from the Goss component, breaking the Cubo-Goss fiber as the deformation increases. On the other hand, when the load is applied in a direction that is parallel to the BD, the texture does not undergo such substantial changes with regard to the initial texture, maintaining the Cubo-Goss fiber and decreasing the dispersion in the components with the increase in deformation, Fig. 14. It should also be noted that when the LD is parallel to the BD, the Copper component begins to form in the BD from the Goss component. Therefore, the breakdown of the cellular network permits the development of more significant changes in texture when the load is applied perpendicular to the BD, as compared to parallel application.

This behavior relates well to the microstructures described in Figs. 6 and 7, in which applying the load on the BD demonstrates the already well-defined orientation of the elongated columnar grains on the BD. On the contrary, the load applied perpendicularly to the BD breaks the texture, possibly changing the grains' shape and orientation. Therefore, it can be inferred that applying the load parallel to BD with the initial elongated grains in this direction leads to an earlier fracture than with perpendicular application. Thus, materials annealed with the load that is applied perpendicularly to the BD register higher sliding activity concerning the as-built material as compared to the load that is parallel to the BD (see plots in Figs. 13 and 14). These marked differences in the sliding activities prove the effect of higher dislocation densities depending on measurement direction and applied load orientation [69].

Using VPSC simulations, we can predict the tensile behavior for different orientations and thus predict the alloy's anisotropy. Fig. 15 indicates the predicted tensile curves for each material together with the Lankford coefficients. Adjusting the model to the experimental curve perpendicular to BD, the behavior for the direction parallel to BD and with a rotation of ~60° around the axis perpendicular to the plane containing the BD (the orientation with the lowest Lankford coefficient) is predicted. In all cases, Fig. 15(a)–15(g) show that the BD and the 60° oriented samples predict the lowest and highest strength in all materials, respectively. Liu et al. [67] also showed that the BD had lower strength

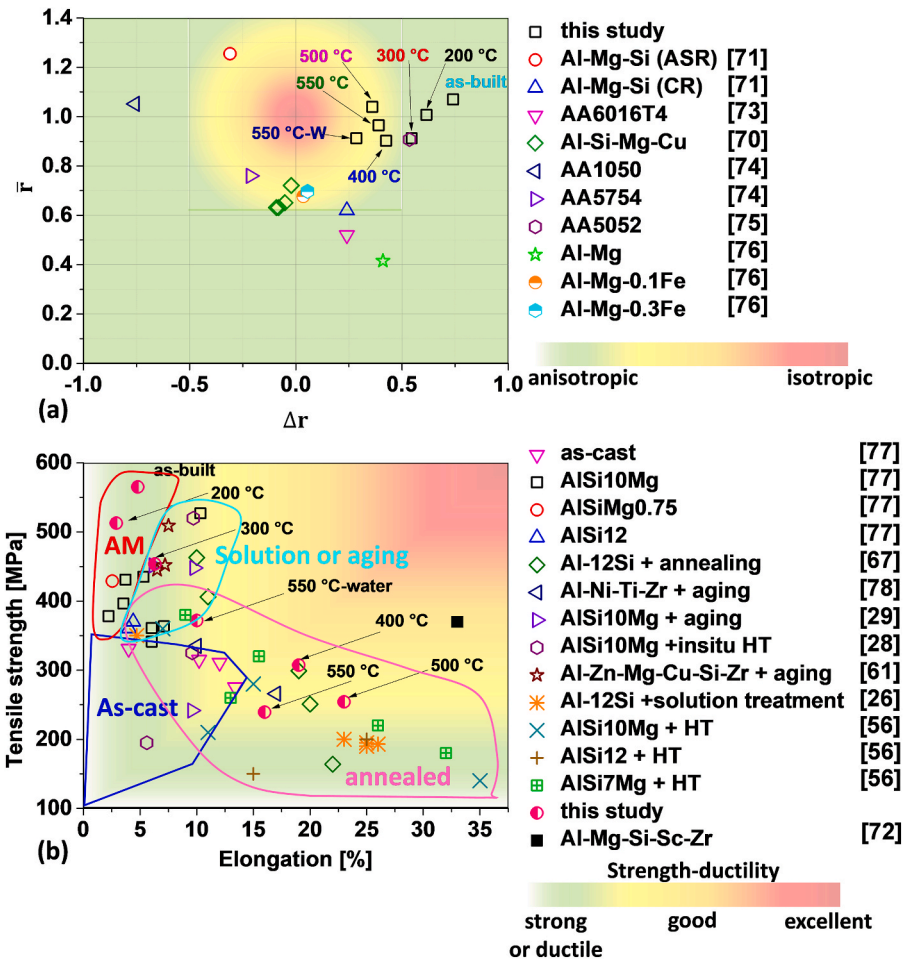

Fig. 16. summary of mechanical properties. (a) average plastic strain ratio vs planar anisotropy for different Al alloys, Al–Mg–Si deformed by ASR and CR [71], AA6016T4 [73], Al-Si-Mg-Cu [70], AA1050 and AA5754 [74], AA5052 [75], Al-Mg [76], Al–Mg-0.1% Fe [76], and Al–Mg-0.3%Fe [76]. (b) mechanical properties comparison for different Al alloys, AlSi10Mg [77], AlSiMg0.75 [77] AlSi12 [77], as-cast [77], Al–12Si + annealing [67], Al–Ni–Ti–Zr + aging [78], AlSi10Mg + aging [29], AlSi10Mg + in-situ HT [28], Al–Zn–Mg–Cu–Si–Zr + aging [61], Al–12Si + solution treatment [26], AlSi10Mg + HT [56], AlSi12 + HT [56], AlSi7Mg + HT [56], and Al–Mg–Si-Sc-Zr [72].

than the perpendicular direction for an Al-12% Si alloy produced by L-PBF. This behavior is related to the Lankford coefficients that describe the anisotropy of the materials as indicated in the insets of Fig. 15 compared to the as-built material. At first glance, the higher the temperature, the lower the Lankford coefficient variation, as indicated by the reduction of the shading between the maximum and minimum of each curve in the insets. This behavior corresponds well to the texture intensity reduction and the development of different components depending on the orientation tested, as seen in Figs. 6, Fig. 13, and Fig. 14. In addition, the decreased scattering on the Lankford coefficients for the heat-treated materials also demonstrates the reduction in differences between the tensile curves.

The evolution of the Lankford coefficients also suggests that the direction perpendicular to the BD has a better formability capacity (i.e., higher Lankford coefficient value) than the BD and that the lowest values are located at 30°–40° from the BD. It is also worth noting that the average plastic strain ratio ($\bar{r}$) and planar anisotropy (Δr) described by the following equations manifest diverse behaviors [70]:

$$\bar{r} = \frac{r_0 + 2r_{45} + r_{90}}{4} \tag{13}$$

$$\Delta r = \frac{r_0 - 2r_{45} + r_{90}}{2} \tag{14}$$

where r_0, r_{45}, and r_{90} represent the Lankford coefficients at the orientations of 0°, 45°, and 90°.

The values of $\bar{r}$ indicated in Fig. 15(a)–15(g) are very similar for all materials varying between 0.9 and 1.07, while the Δr values are much higher in as-built and annealed materials below 300 °C. As of 400 °C and higher, the planar anisotropy values decrease with temperature, revealing that the lower texture intensity and the breakdown of the cellular network give rise to a more isotropic material with $\bar{r}$ values close to 1 and with Δr approaching 0.

When comparing the $\bar{r}$ values of this alloy obtained by L-PBF with those of Al alloys produced by conventional processes, it was found that the as-built alloy plus heat treatments tend to have higher values of $\bar{r}$with lower Δr showing a more isotropic behavior, Fig. 16(a). This figure also shows how alloys subjected to plastic deformation can improve their formability. For example, Miki et al. [71] showed that when using asymmetric rolling (ASR) and conventional cold rolling (CR), the former improved the alloy's formability as a consequence of shear deformations that break the texture, reducing the intensity of the Cube component. Thus, despite the as-built material developing texture components such as Cube, which are not beneficial for improving formability, heat treatments help reduce its intensity, forming components such as Rotated Cube, especially at high temperatures.

The heat treatments for 1 h on the material suggest good strength-ductility relationships compared to various Al alloys obtained by AM subjected to different heat treatments, Fig. 16(b). This figure shows how the as-built alloys present strengths much higher than the as-cast condition, although with reduced ductility. Thus, annealing heat treatments demonstrate that ductility can be improved when maintaining high strengths. Furthermore, heat treatments such as aging or solution treatments have been shown to improve ductility with elongations of 10%, maintaining strengths above 350 MPa. On the other hand, annealing significantly improves ductility, although the decrease in strength begins to be significant, especially for heat treatments involving high temperatures. However, in Fig. 16(b) it can be seen that the alloy

properties after annealing in this study offer good strength-ductility ratios. For example, Liu et al. [67] subjected an AlSi12 alloy to several annealing treatments with temperatures being similar to those of this study, but with a holding time of 2 h, resulting in similar elongations but lower strengths. However, the strength-ductility ratios after heat treatments are not as remarkable as in other studies where, by adding Si and Mg, elongations of over 30% were achieved, along with strengths of over 350 MPa [72]. This work also presents remarkable results in anisotropy reduction, one of the problems of great interest in alloys obtained by AM.

Therefore, L-PBF permits the generation of an Al alloy having properties superior to those obtained by traditional processes due to the creation of microstructures made up of a Si-rich interconnected network, a heterogeneous grain size distribution, and high density of dislocations. However, the stiffness of the Si network and the strong texture generate low ductility and anisotropy. Therefore, heat treatments generate various properties with different ductility and strength while reducing anisotropy with increasing temperature.

4. Conclusions

By subjecting a hypoeutectic AlSi11Cu alloy to different heat treatments after the manufacturing process, the following conclusions can be reached:

1) The alloy presented a structure formed by an Al matrix surrounded by a network enriched in Si. This network demonstrated stability up to temperatures of 300 °C. Above this temperature, the interconnected network breaks, generating uniformly distributed particles that grow due to the migration of Si in solid solution and the absorption of neighboring particles.
2) The manufacturing process generated a heterogeneous microstructure formed by equiaxed and large grains with columnar morphology, maintained after the heat treatments. In addition, the texture studies demonstrated the dominance of recrystallization components such as Goss and Cube. This indicates the preservation of the grain boundary strengthening component as confirmed by the small changes in misorientation and grain sizes after heat treatments.
3) It was possible to improve the alloy's ductility through heat treatments at the cost of reducing its strength, indicating a broad scope of properties depending on the temperature and the cooling medium. For example, after annealing at 500 °C, tensile strength was over 200 MPa, with a final fracture strain close to 25%. On the other hand, quenching at 550 °C led to an attractive combination of strength and ductility (400 MPa maximum stress and 10% fracture strain).
4) Strength deterioration with the heat treatments is associated with different factors such as the breakdown of the Si-rich interconnected network and the migration of Si in the solid solution towards the particles that remain from the network breaking, causing them to grow with the temperature increase affecting the solid solution and precipitates hardening mechanisms.
5) VSPC simulation determined that the as-built alloy with the BD parallel to the longitudinal axis of the bars presented high strengths when the load was applied at 30° with regard to BD and the lowest strength when applied perpendicular to the BD. According to Lankford coefficients, this predicted anisotropy effect was more pronounced in the as-built material and decreased as the temperature of the heat treatments increased.

Credit authorship contribution statement

Jairo Alberto Muñoz: Investigation, Formal analysis, Writing original draft, Writing review and editing. **Sergio Elizalde:** Investigation, Data curation. **Alexander Komissarov:** Supervision, Funding acquisition. **José María Cabrera:** Writing review and editing, Funding acquisition.

Declaration of competing interest

The authors declare that they have no known competing financial interests or personal relationships that could have appeared to influence the work reported in this paper.

Data availability

Data will be made available on request.

Acknowledgements

The authors thank Professor Javier Walter Signorelli from the Instituto de Física Rosario in Rosario, Argentina, for his help using the VPSC model.

Appendix A. Supplementary data

Supplementary data to this article can be found online at https://doi.org/10.1016/j.msea.2022.144091.

References

[1] J. Podroužek, M. Marcon, K. Ninčević, R. Wan-Wendner, Bio-inspired 3D infill patterns for additive manufacturing and structural applications, Materials 12 (2019), https://doi.org/10.3390/ma12030499.
[2] A. Paolini, S. Kollmannsberger, E. Rank, Additive manufacturing in construction: a review on processes, applications, and digital planning methods, Addit. Manuf. 30 (2019), 100894, https://doi.org/10.1016/j.addma.2019.100894.
[3] D. Delgado Camacho, P. Clayton, W.J. O'Brien, C. Seepersad, M. Juenger, R. Ferron, S. Salamone, Applications of additive manufacturing in the construction industry - a forward-looking review, Autom. ConStruct. 89 (2018) 110–119, https://doi.org/10.1016/j.autcon.2017.12.031.
[4] T.D. Ngo, A. Kashani, G. Imbalzano, K.T.Q. Nguyen, D. Hui, Additive manufacturing (3D printing): a review of materials, methods, applications and challenges, Compos. B Eng. 143 (2018) 172–196, https://doi.org/10.1016/j.compositesb.2018.02.012.
[5] M. Attaran, The rise of 3-D printing: the advantages of additive manufacturing over traditional manufacturing, Bus. Horiz. 60 (2017) 677–688, https://doi.org/10.1016/j.bushor.2017.05.011.
[6] J. Jiang, X. Xu, J. Stringer, Support structures for additive manufacturing: a review, J. Manuf. Mater. Process. 2 (2018), https://doi.org/10.3390/jmmp2040064.
[7] J. Gunasekaran, P. Sevvel, I. John Solomon, Metallic materials fabrication by selective laser melting: a review, Mater. Today Proc. 37 (2021) 252–256, https://doi.org/10.1016/j.matpr.2020.05.162.
[8] Z. Alomar, F. Concli, A review of the selective laser melting lattice structures and their numerical models, Adv. Eng. Mater. 22 (2020), 2000611, https://doi.org/10.1002/adem.202000611.
[9] C.Y. Yap, C.K. Chua, Z.L. Dong, Z.H. Liu, D.Q. Zhang, L.E. Loh, S.L. Sing, Review of selective laser melting: materials and applications, Appl. Phys. Rev. 2 (2015), 41101, https://doi.org/10.1063/1.4935926.
[10] W.S.W. Harun, K. Kadirgama, M. Samykano, D. Ramasamy, I. Ahmad, M. Moradi, 5 - mechanical behavior of selective laser melting-produced metallic biomaterials, in: J.P. Davim (Ed.), Mech. Behav. Biomater, Woodhead Publishing, 2019, pp. 101–116, https://doi.org/10.1016/B978-0-08-102174-3.00005-X.
[11] M.J. Ansari, D.-S. Nguyen, H.S. Park, Investigation of SLM process in terms of temperature distribution and melting pool size: modeling and experimental approaches, Materials 12 (2019), https://doi.org/10.3390/ma12081272.
[12] G.M. Karthik, H.S. Kim, Heterogeneous aspects of additive manufactured metallic parts: a review, Met. Mater. Int. 27 (2021) 1–39, https://doi.org/10.1007/s12540-020-00931-2.
[13] X.X. Zhang, H. Andrä, S. Harjo, W. Gong, T. Kawasaki, A. Lutz, M. Lahres, Quantifying internal strains, stresses, and dislocation density in additively manufactured AlSi10Mg during loading-unloading-reloading deformation, Mater. Des. 198 (2021), 109339, https://doi.org/10.1016/j.matdes.2020.109339.
[14] J.A. Muñoz, M. Pavlov, V. Cheverikin, A. Komissarov, A. Gromov, Heterogeneity consequences on the mechanical and microstructural evolution of an AlSi11Cu alloy obtained by selective laser melting, Mater. Char. 174 (2021), 110989, https://doi.org/10.1016/j.matchar.2021.110989.
[15] Z. Sun, X. Tan, S.B. Tor, W.Y. Yeong, Selective laser melting of stainless steel 316L with low porosity and high build rates, Mater. Des. 104 (2016) 197–204, https://doi.org/10.1016/j.matdes.2016.05.035.
[16] L. Thijs, F. Verhaeghe, T. Craeghs, J. Van Humbeeck, J.-P. Kruth, A study of the microstructural evolution during selective laser melting of Ti-6Al-4V, Acta Mater. 58 (2010) 3303–3312, https://doi.org/10.1016/j.actamat.2010.02.004.
[17] C. Zhao, Z. Wang, D. Li, L. Kollo, Z. Luo, W. Zhang, K.G. Prashanth, Selective laser melting of Cu-Ni-Sn: a comprehensive study on the microstructure, mechanical properties, and deformation behavior, Int. J. Plast. 138 (2021), 102926, https://doi.org/10.1016/j.ijplas.2021.102926.

[18] F.C. Robles Hernandez, J.M. Herrera Ramírez, R. Mackay, Applications in the automotive and aerospace industries, in: Al-Si Alloy. Automotive, Aeronaut. Aerosp. Appl, Springer International Publishing, Cham, 2017, pp. 163–171, https://doi.org/10.1007/978-3-319-58380-8_7.
[19] N. Read, W. Wang, K. Essa, M.M. Attallah, Selective laser melting of AlSi10Mg alloy: process optimisation and mechanical properties development, Mater. Des. 65 (2015) 417–424, https://doi.org/10.1016/j.matdes.2014.09.044.
[20] X. Liu, C. Zhao, X. Zhou, Z. Shen, W. Liu, Microstructure of selective laser melted AlSi10Mg alloy, Mater. Des. 168 (2019), 107677 doi.org/10.1016/j.matdes.2019.107677.
[21] F. Yan, W. Xiong, E.J. Faierson, Grain structure control of additively manufactured metallic materials, Materials 10 (2017), https://doi.org/10.3390/ma10111260.
[22] L. Hitzler, J. Hirsch, B. Heine, M. Merkel, W. Hall, A. Öchsner, On the anisotropic mechanical properties of selective laser-melted stainless steel, Materials 10 (2017), https://doi.org/10.3390/ma10101136.
[23] Y. Kok, X.P. Tan, P. Wang, M.L.S. Nai, N.H. Loh, E. Liu, S.B. Tor, Anisotropy and heterogeneity of microstructure and mechanical properties in metal additive manufacturing: a critical review, Mater. Des. 139 (2018) 565–586, doi.org/10.1016/j.matdes.2017.11.021.
[24] J. Delahaye, J.T. Tchuindjang, J. Lecomte-Beckers, O. Rigo, A.M. Habraken, A. Mertens, Influence of Si precipitates on fracture mechanisms of AlSi10Mg parts processed by Selective Laser Melting, Acta Mater. 175 (2019) 160–170, doi.org/10.1016/j.actamat.2019.06.013.
[25] Z.H. Xiong, S.L. Liu, S.F. Li, Y. Shi, Y.F. Yang, R.D.K. Misra, Role of melt pool boundary condition in determining the mechanical properties of selective laser melting AlSi10Mg alloy, Mater. Sci. Eng. (2019) 740–741, 148–156. doi.org/10.1016/j.msea.2018.10.083.
[26] X.P. Li, X.J. Wang, M. Saunders, A. Suvorova, L.C. Zhang, Y.J. Liu, M.H. Fang, Z. H. Huang, T.B. Sercombe, A selective laser melting and solution heat treatment refined Al-12Si alloy with a controllable ultrafine eutectic microstructure and 25% tensile ductility, Acta Mater. 95 (2015) 74–82, https://doi.org/10.1016/j.actamat.2015.05.017.
[27] L. Zhao, J.G. Santos Macías, L. Ding, H. Idrissi, A. Simar, Damage mechanisms in selective laser melted AlSi10Mg under as built and different post-treatment conditions, Mater. Sci. Eng. 764 (2019), 138210, https://doi.org/10.1016/j.msea.2019.138210.
[28] J.G. Santos Macías, T. Douillard, L. Zhao, E. Maire, G. Pyka, A. Simar, Influence on microstructure, strength and ductility of build platform temperature during laser powder bed fusion of AlSi10Mg, Acta Mater. 201 (2020) 231–243, doi.org/10.1016/j.actamat.2020.10.001.
[29] T.-H. Park, M.-S. Baek, H. Hyer, Y. Sohn, K.-A. Lee, Effect of direct aging on the microstructure and tensile properties of AlSi10Mg alloy manufactured by selective laser melting process, Mater. Char. 176 (2021), 111113, https://doi.org/10.1016/j.matchar.2021.111113.
[30] A. Kempf, K. Hilgenberg, Influence of heat treatments on AlSi10Mg specimens manufactured with different laser powder bed fusion machines, Mater. Sci. Eng. 818 (2021), 141371 doi.org/10.1016/j.msea.2021.141371.
[31] Y.K. Xiao, H. Chen, Z.Y. Bian, T.T. Sun, H. Ding, Q. Yang, Y. Wu, Q. Lian, Z. Chen, H.W. Wang, Enhancing strength and ductility of AlSi10Mg fabricated by selective laser melting by TiB2 nanoparticles, J. Mater. Sci. Technol. 109 (2022) 254–266, doi.org/10.1016/j.jmst.2021.08.030.
[32] F. Bosio, P. Fino, D. Manfredi, M. Lombardi, Strengthening strategies for an Al alloy processed by in-situ alloying during laser powder bed fusion, Mater. Des. 212 (2021), 110247 doi.org/10.1016/j.matdes.2021.110247.
[33] M. Liu, N. Takata, A. Suzuki, M. Kobashi, Effect of heat treatment on gradient microstructure of AlSi10Mg lattice structure manufactured by laser powder bed fusion, Materials 13 (2020), https://doi.org/10.3390/ma13112487.
[34] A.V. Pozdniakov, A.Y. Churyumov, I.S. Loginova, D.K. Daubarayte, D.K. Ryabov, V. A. Korolev, Microstructure and properties of novel AlSi11CuMn alloy manufactured by selective laser melting, Mater. Lett. 225 (2018) 33–36, doi.org/10.1016/j.matlet.2018.04.077.
[35] A.Y. Nalivaiko, D.Y. Ozherelkov, I.A. Pelevin, S.V. Chernyshikhin, A.E. Medvedev, A.V. Korshunov, A.N. Arnautov, A.A. Gromov, Comprehensive study of the 3D printing of single tracks and cubic samples by selective laser melting of AlSi10MgCu alloy, Met. Mater. Int. (2022), https://doi.org/10.1007/s12540-021-01115-2.
[36] J. Fiocchi, A. Tuissi, C.A. Biffi, Heat treatment of aluminium alloys produced by laser powder bed fusion: a review, Mater. Des. 204 (2021), 109651 doi.org/10.1016/j.matdes.2021.109651.
[37] R. Rashid, S.H. Masood, D. Ruan, S. Palanisamy, R.A. Rahman Rashid, J. Elambasseril, M. Brandt, Effect of energy per layer on the anisotropy of selective laser melted AlSi12 aluminium alloy, Addit. Manuf. 22 (2018) 426–439, doi.org/10.1016/j.addma.2018.05.040.
[38] S. Bai, N. Perevoshchikova, Y. Sha, X. Wu, The effects of selective laser melting process parameters on relative density of the AlSi10Mg parts and suitable procedures of the archimedes method, Appl. Sci. 9 (2019), https://doi.org/10.3390/app9030583.
[39] D.Y. Ozherelkov, A.Y. Nalivaiko, A.A. Gromov, D.O. Solodov, A.A. Komissarov, A. S. Shinkaryov, A.I. Morozova, On the formation of AlSiMgCu/quasicrystal powder composite single tracks by selective laser melting, IOP Conf. Ser. Mater. Sci. Eng. 1014 (2021), 12032, https://doi.org/10.1088/1757-899x/1014/1/012032.
[40] C. Igathinathane, L.O. Pordesimo, E.P. Columbus, W.D. Batchelor, S.R. Methuku, Shape identification and particles size distribution from basic shape parameters using ImageJ, Comput. Electron. Agric. 63 (2008) 168–182, https://doi.org/10.1016/j.compag.2008.02.007.
[41] J.A. Muñoz, M. Melia, M. Avalos, R.E. Bolmaro, Equal channel angular sheet extrusion (ECASE) produces twinning heterogeneity in commercially pure titanium, Mater. Char. 181 (2021), 111460 doi.org/10.1016/j.matchar.2021.111460.
[42] R.A. Lebensohn, C.N. Tomé, A self-consistent anisotropic approach for the simulation of plastic deformation and texture development of polycrystals: application to zirconium alloys, Acta Metall. Mater. 41 (1993) 2611–2624, doi.org/10.1016/0956-7151(93)90130-K.
[43] C. Tome, G.R. Canova, U.F. Kocks, N. Christodoulou, J.J. Jonas, The relation between macroscopic and microscopic strain hardening in F.C.C. polycrystals, Acta Metall. 32 (1984) 1637–1653, doi.org/10.1016/0001-6160(84)90222-0.
[44] B.S. Anglin, B.T. Gockel, A.D. Rollett, Developing constitutive model parameters via a multi-scale approach, Integr. Mater. Manuf. Innov. 5 (2016) 212–231, https://doi.org/10.1186/s40192-016-0053-4.
[45] Y.J. Liu, Z. Liu, Y. Jiang, G.W. Wang, Y. Yang, L.C. Zhang, Gradient in microstructure and mechanical property of selective laser melted AlSi10Mg, J. Alloys Compd. 735 (2018) 1414–1421, doi.org/10.1016/j.jallcom.2017.11.020.
[46] I. Rosenthal, A. Stern, N. Frage, Microstructure and mechanical properties of AlSi10Mg parts produced by the laser beam additive manufacturing (AM) technology, Metallogr. Microstruct. Anal. 3 (2014) 448–453, https://doi.org/10.1007/s13632-014-0168-y.
[47] J. Alberto Muñoz, A. Komissarov, M. Avalos, R.E. Bolmaro, Heat treatment effect on an AA6063 alloy, Mater. Lett. 277 (2020), 128338 doi.org/10.1016/j.matlet.2020.128338.
[48] J.A. Muñoz, M. Avalos, R.E. Bolmaro, Heterogeneity of strain path, texture and microstructure evolution of AA6063-T6 processed by Equal Channel Angular Sheet Extrusion (ECASE), J. Alloys Compd. 768 (2018) 349–357, https://doi.org/10.1016/j.jallcom.2018.07.216.
[49] B. Bacroix, S. Queyreau, D. Chaubet, E. Siv, T. Chauveau, The influence of the cube component on the mechanical behaviour of copper polycrystalline samples in tension, Acta Mater. 160 (2018) 121–136, doi.org/10.1016/j.actamat.2018.08.044.
[50] J. Wu, X.Q. Wang, W. Wang, M.M. Attallah, M.H. Loretto, Microstructure and strength of selectively laser melted AlSi10Mg, Acta Mater. 117 (2016) 311–320, doi.org/10.1016/j.actamat.2016.07.012.
[51] U. Tradowsky, J. White, R.M. Ward, N. Read, W. Reimers, M.M. Attallah, Selective laser melting of AlSi10Mg: influence of post-processing on the microstructural and tensile properties development, Mater. Des. 105 (2016) 212–222, doi.org/10.1016/j.matdes.2016.05.066.
[52] N.T. Aboulkhair, N.M. Everitt, I. Ashcroft, C. Tuck, Reducing porosity in AlSi10Mg parts processed by selective laser melting, Addit. Manuf. 1–4 (2014) 77–86, doi.org/10.1016/j.addma.2014.08.001.
[53] A.S. Haselhuhn, P.G. Sanders, J.M. Pearce, Hypoeutectic aluminum-silicon alloy development for GMAW-based 3-D printing using wedge castings, Int. J. Med. 11 (2017) 843–856, https://doi.org/10.1007/s40962-017-0133-z.
[54] S. Swaminathan, J.M. García-Infanta, T.R. McNelley, O.A. Ruano, F. Carreño, Severe plastic deformation of an as-cast hypoeutectic Al-Si alloy, J. Mater. Sci. 43 (2008) 7501–7506, https://doi.org/10.1007/s10853-008-2625-y.
[55] W. Chen, T. Voisin, Y. Zhang, J.-B. Florien, C.M. Spadaccini, D.L. McDowell, T. Zhu, Y.M. Wang, Microscale residual stresses in additively manufactured stainless steel, Nat. Commun. 10 (2019) 4338, https://doi.org/10.1038/s41467-019-12265-8.
[56] N.T. Aboulkhair, M. Simonelli, L. Parry, I. Ashcroft, C. Tuck, R. Hague, 3D printing of Aluminium alloys: additive Manufacturing of Aluminium alloys using selective laser melting, Prog. Mater. Sci. 106 (2019), 100578 doi.org/10.1016/j.pmatsci.2019.100578.
[57] Y. Li, K. Zhou, P. Tan, S.B. Tor, C.K. Chua, K.F. Leong, Modeling temperature and residual stress fields in selective laser melting, Int. J. Mech. Sci. 136 (2018) 24–35, doi.org/10.1016/j.ijmecsci.2017.12.001.
[58] J.A. Muñoz, M. Avalos, N. Schell, H.G. Brokmeier, R.E. Bolmaro, Comparison of a low carbon steel processed by Cold Rolling (CR) and Asymmetrical Rolling (ASR): heterogeneity in strain path, texture, microstructure and mechanical properties, J. Manuf. Process. 64 (2021) 557–575, doi.org/10.1016/j.jmapro.2021.02.017.
[59] F. Czerwinski, Thermal stability of aluminum alloys, Mater. (Basel, Switzerland) 13 (2020) 3441, https://doi.org/10.3390/ma13153441.
[60] D. Song, G. Wang, Z. Zhou, E.E. Klu, B. Gao, A. Ma, Y. Wu, J. Sun, J. Jiang, X. Ma, Developing a high-strength Al-11Si alloy with improved ductility by combining ECAP and cryorolling, Mater. Sci. Eng. 773 (2020), 138880, https://doi.org/10.1016/j.msea.2019.138880.
[61] L. Li, T. Yuan, C. Deng, D. Zheng, Effects of aging treatment on microstructure and mechanical properties of selective laser melted Al-Zn-Mg-Cu-Si-Zr alloys, J. Alloys Compd. 890 (2022), 161810 doi.org/10.1016/j.jallcom.2021.161810.
[62] Z.W. Du, Z.M. Sun, B.L. Shao, T.T. Zhou, C.Q. Chen, Quantitative evaluation of precipitates in an Al-Zn-Mg-Cu alloy after isothermal aging, Mater. Char. 56 (2006) 121–128, doi.org/10.1016/j.matchar.2005.10.004.
[63] X.X. Zhang, A. Lutz, H. Andrä, M. Lahres, D. Sittig, E. Maawad, W.M. Gan, D. Knoop, An additively manufactured and direct-aged AlSi3.5Mg2.5 alloy with superior strength and ductility: micromechanical mechanisms, Int. J. Plast. 146 (2021), 103083 doi.org/10.1016/j.ijplas.2021.103083.
[64] D. Canelo-Yubero, C. Etzlstorfer, R. Koos, H. Germann, T. Steffens, A. Stark, E. Boller, G. Requena, Load partition during hot deformation of AlSi12 and AlSi10Cu6Ni2 alloys: a quantitative evaluation of the stiffness of Si networks, J. Mater. Sci. 55 (2020) 14558–14570, https://doi.org/10.1007/s10853-020-05023-5.

[65] G. Wang, H. Ouyang, C. Fan, Q. Guo, Z. Li, W. Yan, Z. Li, The origin of high-density dislocations in additively manufactured metals, Mater. Res. Lett. 8 (2020) 283–290, https://doi.org/10.1080/21663831.2020.1751739.
[66] T. Khelfa, R. Lachhab, H. Azzeddine, Z. Chen, J.A. Muñoz, J.M. Cabrera-Marrero, F. Brisset, A.-L. Helbert, T. Baudin, M. Khitouni, Effect of ECAP and subsequent annealing on microstructure, texture, and microhardness of an AA6060 aluminum alloy, J. Mater. Eng. Perform. (2021), https://doi.org/10.1007/s11665-021-06404-w.
[67] M. Liu, T. Wada, A. Suzuki, N. Takata, M. Kobashi, M. Kato, Effect of annealing on anisotropic tensile properties of Al-12%Si alloy fabricated by laser powder bed fusion, Crystals 10 (2020), https://doi.org/10.3390/cryst10111007.
[68] J.A. Muñoz Bolaños, D. Ten, B. Viacheslav, A. Komissarov, A. Gromov, Mechanical and microstructural evolution of a 3D printed AlSi11Cu alloy, Procedia CIRP 95 (2020) 103–108, doi.org/10.1016/j.procir.2020.03.132.
[69] J.A. Muñoz, J.M. Cabrera, Effect of loading mode on the microstructural heterogeneity of ultra-fine-grained iron, Mater. Lett. 304 (2021), 130630 doi.org/10.1016/j.matlet.2021.130630.
[70] J.G. Jeon, J.H. Shin, S.E. Shin, D.H. Bae, Improvement in the anisotropic mechanical properties and formability of Al-Si-Mg-Cu-based alloy sheets, Mater. Sci. Eng. 799 (2021), 140199 doi.org/10.1016/j.msea.2020.140199.
[71] Y. Miki, O. Noguchi, Y. Ueno, Y. Suzuki, K. Koyama, T. Komatsubara, Improvement of deep drawability of Al-Mg-Si alloy sheets for automotive panel by asymmetric warm rolling, in: Proc. 12th Int. Conf. Alum. Alloy, 2010, pp. 5–9. Yokohama, Japan.
[72] R. Li, M. Wang, Z. Li, P. Cao, T. Yuan, H. Zhu, Developing a high-strength Al-Mg-Si-Sc-Zr alloy for selective laser melting: crack-inhibiting and multiple strengthening mechanisms, Acta Mater. 193 (2020) 83–98, doi.org/10.1016/j.actamat.2020.03.060.
[73] M. Lenzen, M. Merklein, Analysis of the Lankford coefficient evolution at different strain rates for AA6016-T4, DP800 and DC06, AIP Conf. Proc. 1896 (2017), 160001, https://doi.org/10.1063/1.5008176.
[74] S. Olguner, A.T. Bozdana, Prediction of Lankford coefficients for AA1050 and AA5754 aluminum sheets using uniaxial tensile tests and cup drawing experiments, in: V. Ivanov, J. Trojanowska, J. Machado, O. Liaposhchenko, J. Zajac, I. Pavlenko, M. Edl, D. Perakovic (Eds.), Adv. Des. Simul. Manuf. II, Springer International Publishing, Cham, 2020, pp. 438–446.
[75] H.H. Nguyen, H.C. Vu, Forming limit prediction of anisotropic aluminum magnesium alloy sheet AA5052-H32 using micromechanical damage model, J. Mater. Eng. Perform. 29 (2020) 4677–4691, https://doi.org/10.1007/s11665-020-04987-4.
[76] H. Inoue, T. Takasugi, Texture control for improving deep drawability in rolled and annealed aluminum alloy sheets, Mater. Trans. 48 (2007) 2014–2022, https://doi.org/10.2320/matertrans.L-MRA2007871.
[77] H. Wu, Y. Ren, J. Ren, L. Liang, R. Li, Q. Fang, A. Cai, Q. Shan, Y. Tian, I. Baker, Selective laser melted AlSi10Mg alloy under melting mode transition: microstructure evolution, nanomechanical behaviors and tensile properties, J. Alloys Compd. 873 (2021), 159823 doi.org/10.1016/j.jallcom.2021.159823.
[78] S. Thapliyal, S. Shukla, L. Zhou, H. Hyer, P. Agrawal, P. Agrawal, M. Komarasamy, Y. Sohn, R.S. Mishra, Design of heterogeneous structured Al alloys with wide processing window for laser-powder bed fusion additive manufacturing, Addit. Manuf. 42 (2021), 102002 doi.org/10.1016/j.addma.2021.102002.